UNIVERSIDAD POLITECNICA DE VALENCIA

DEPARTAMENTO DE COMUNICACIONES

Máster Universitario en Tecnologías, Sistemas y Redes de Comunicaciones

True-Time Delay Lines Based on Multicore Optical Fibers

Author: Sergi García Cortijo

Director 1: José Capmany Francoy

Director 2: Ivana Gasulla Mestre

Course: 2014-2015

Workplace: Optical and quantum communication group (GCOC), iTEAM

Objectives — The main purpose of this work is to properly design the cores of a multicore fiber in order to build sampled true-time delay lines based on multicore optical fibers. Since inter-core crosstalk is one of the most limiting effects in multicore fibers, we must take it into account and characterize it with the aim of applying different techniques to avoid it or at least mitigate its impact. Once the true-time delay lines are designed, they can be included into several microwave photonics applications such as microwave optical filters, optoelectronic oscillators, etc.

Methodology — The methodology of this work can be divided in two parts. First, it was necessary to perform a comprehensive study of the main concepts related to multicore fibers and several microwave photonics applications, especially focused towards inter-core crosstalk and true-time delay lines. The second part of the work is based on simulation activity carried out by using the simulation software named *Fimmwave*, which allows us to do a versatile design of the multicore fiber and also different evaluations of our designs, including the evaluation of several parameters of the cores such as the dispersion, the group index or the effective index, and also a rigorous inter-core crosstalk analysis. Additional simulations are also done using *Matlab*.

Theoretical developments realized — During this work, a theoretical model of multi-cavity optoelectronic oscillators using multicore fibers has been developed, which includes both signal and noise theoretical models.

Results — Different results have been obtained during this work. With respect to the design of true-time delay lines based on multicore fiber, we proposed an unprecedented design procedure for the refractive index profile of the cores in order to ensure a desired group index, effective index and dispersion parameter in each core. We demonstrate the feasibility of the proposed models by implementing three different designs, for which we evaluate both crosstalk versus propagation length and crosstalk versus bending radius behaviors. Regarding to the optoelectronic oscillators, we propose three different models, two of them based on homogeneous multicore fibers and the last one based on heterogeneous multicore fibers. In all cases, we evaluated and compared the oscillation frequencies and the phase noise of the optoelectronic oscillator in different situations.

Future lines — The most straightforward future line is the physical implementation in the laboratory of different microwave photonics applications as, for example, the optoelectronic oscillator models. The main obstacle to do this is the acquisition of the desired multicore fibers because of its high prize and the difficulty to obtain a specific design.

Publications — Three articles have been published (one of them not yet published, but accepted) that report the results of this work. Firstly, we publish a paper in Optics Letters where we propose the novel design of true-time delay lines based on multicore fibers. Almost simultaneously, the optoelectronic oscillator results were also published in Optics Express. A third and last publication is not yet published, but it is accepted.

This one is related to the first one, where we optimize the proposed models in order to minimize the inter-core crosstalk and the behavior against curvatures of the multicore fiber, and we also presented some simulation results illustrating the comparative between models.

Abstract — In this work, we propose a novel design of true-time delay lines based on multicore fibers. First, a brief introduction to microwave photonics and multicore fibers is exposed in order to make sure that the reader knows the basic concepts to understand the proposed designs. After that, the desired true-time delay lines are described. Here, three different models are proposed, which can be distinguished by their core's refractive index profile: one based on a step-index profile, and two based on a trench-assisted step index profile. In all cases, both crosstalk versus propagation length and crosstalk versus bending radius simulations are exposed. Finally, we make use of the proposed concept to implement three different models of optoelectronic oscillators, depending on which homogeneous or heterogeneous multicore fibers are employed to build the delay line. Those models are then evaluated in terms of oscillation frequencies and phase noise.

Author: Sergi García Cortijo, email: sergarc3@teleco.upv.es
Director 1: José Capmany Francoy, email: jcapmany@iteam.upv.es
Director 2: Ivana Gasulla Mestre, email: ivgames@iteam.upv.es
Delivery date: 07-09-15

ÍNDICE

I. INTRODUCTION

Microwave Photonics (MWP) is an interdisciplinary area that brings together the worlds of radiofrequency (RF) and optoelectronics, granting a promising future in applications such as broadband communications, distributed sensing, security and medical imaging. It pursues the generation, processing and distribution of microwave and millimeter-wave signals by photonic means. Compared to traditional RF technologies, MWP brings unique advantages inherent to photonics engineering, such as low loss (independent of the radio frequency), high bandwidth or immunity to electromagnetic interference. In addition, it also enables key features such as fast tunability and reconfigurability that are not possible using classic electronic approaches. These attractive properties are behind the intense research activity on a wide range of information and communication solutions, including microwave signal filtering, optical beamforming for phased-array antennas, arbitrary waveform generation, multi-gigabit per second analog-to-digital conversion and optoelectronic oscillation, [1-4]. Most of these approaches rely on a core optical component: the true time-delay line (TTDL). Different photonic technology approaches have been reported for the implementation of this essential device. Solutions based on single-core single-mode fibers, which include both passive (switched and dispersive fibers [5] and Fiber Bragg Grating inscription [6-8]) and active [9] (based on Stimulated Brillouin Scattering) configurations featured operation bandwidths and delays between 0.1-10 GHz and 0.4-8 ns, respectively. On the other hand, integrated photonic approaches based on ring cavities in Silicon on Insulator [10], racetrack resonators in Si_3N_4 [10], photonic crystal structures [11] and amplifiers [12] based on InP have demonstrated operation bandwidths and delays between 2-50 GHz and 40-140 ps, respectively.

Despite the immense application potential of MWP in both civil and defense scenarios, as well as the recent claim that it can be extended to emerging fields such as the *Internet of Things*, medical imaging, optical coherence tomography, wireless personal area networks and converged fiber-wireless access networks, the widespread adoption of MWP is still limited by the non-compact, heavy and power-consuming nature of the up-to-date systems. Therefore, one of the major challenges that MWP has to overcome nowadays is related to the reduction of size, weight and power consumption (SWAP) while assuring broadband seamless reconfigurability and stability. Integrated MWP has recently been proposed as a solution for the generation and signal processing of microwave and millimeter-wave signals, but there is still a paramount need for a compact and efficient fiber-based technology able to support the required parallelization in distribution networks. This second scenario, which includes applications such as 5G fiber-wireless access networks and fiber-to-the-home, usually resorts to the "force-brute" replication of a basic subsystem that includes the same single functionality, where the TTDL is built from discrete and bulky components. To overcome this limitation and provide the required component count

reductions and system parallelization, the extension of space-division multiplexing (SDM) techniques, currently restricted to high-capacity digital communications, to the field of MWP was proposed in [13] by the use of heterogeneous multicore fibers (MCF). The inherent parallelism of MCFs makes them ideal candidates for the implementation of sampled discrete TTDLs featuring unique properties in terms of compactness, system stability, power efficiency, flexibility, versatility and record bandwidth in a single compact optical fiber. Fig. 1 illustrates the basic operation principle of the proposed TTDLs working over a single RF-modulated optical carrier.

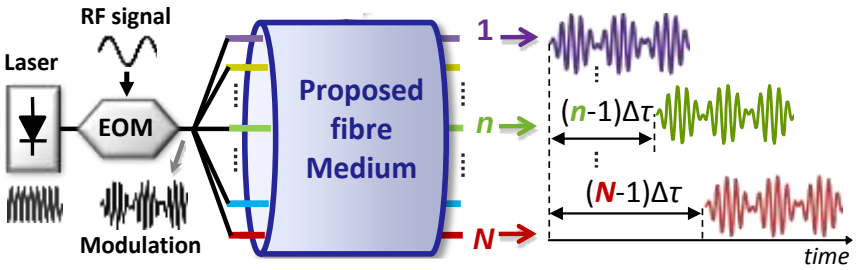

Fig. 1. TTDL based on a heterogeneous MCF fed by a single optical carrier (1D operation).

Most of the research activity on SDM has employed the so-called homogeneous MCFs, where N identical single-mode cores are arranged into a single cladding with an outer diameter ranging from 125 to 250 μm. In this kind of MCF, the number of cores that can be multiplexed into a fiber is determined by the core pitch (i.e., the core-to-core distance) for a fixed outer cladding diameter. However, a small core pitch results in a large crosstalk between neighboring cores, being an important limitation to the core packing density in homogeneous MCFs. In this context, heterogeneous MCFs were proposed in 2009 in order to increase the core packing density as compared to conventional homogeneous MCFs, [14]. These are composed of non-identical cores confined inside a cladding so, since each core has different propagation constant, the phase-matching condition between this dissimilar cores is prevented and thus the inter-core crosstalk becomes sufficiently small to allow an important core pitch reduction, [14-19]. Preliminary designs of heterogeneous MCFs reached crosstalk values below -30 dB for a propagation length of 100 km by arranging 2 or 3 kinds of cores inside a 125-μm cladding diameter, [14]. In that work, by reducing the core pitch and radius while increasing the relative refractive index difference between cores, 12-core and 19-core designs were presented. Further progress in crosstalk management has been achieved by designing heterogeneous trench-assisted core configurations, where crosstalk values near -50 dB for a 100-km link were obtained in a 14-core structure [15]. One of the major design issues regarding the crosstalk management of heterogeneous MCFs is associated to the fiber curvatures that may affect the deployed link. Since phase-matching conditions between non-identical cores may occur when the fiber is curved, the power transfer between cores may increase for a specific range of bending radii. To assure a bend-insensitive behavior, the MCF must be designed so that the cable bending radius is greater than the threshold bending radius R_{pk}, for which

the effective index difference between cores becomes zero. Previous research anticipated that it is possible to shift R_{pk} below 50 mm by designing neighboring cores with an effective index difference larger than 0.001 for a core pitch below 35 μm [15].

II. MULTICORE OPTICAL FIBERS

Multicore fibers are optical fibers where multiple cores are multiplexed into a single cladding. They can be classified in two types according to the desired behavior between their cores: coupled and uncoupled MCFs. For our purpose, we will make use of the uncoupled ones, where each core acts as an independent single-mode waveguide. Depending on the core's design, there are mainly two types of uncoupled MCFs: homogeneous and heterogeneous multicore fibers. Homogeneous MCFs are composed of identical cores which have the same core radius and refractive index profile, while heterogeneous MCFs are characterized by the insertion of dissimilar cores into the same cladding, [21].

Next sections are focused on how inter-core crosstalk affects to both homogeneous and heterogeneous MCFs and how can it be suppressed in order to guarantee a required crosstalk level to transmit along a given propagation length.

II.1. *INTER-CORE CROSSTALK*

In optical fibers, core and cladding geometries are not perfectly circular along the z-axis, and the refractive index also suffers light and inevitable variations along the same axis. All this variations can be understood as a perturbation of the refractive index, causing that the propagating modes of the MCF cores stop being independent one of each other and exchange power along their propagation. Moreover, bending and twisting the fiber along z-axis can also be interpreted as a perturbation of the refractive index of each MCF core, causing the same effect than before. This phenomenon of power exchange receives the name of **inter-core crosstalk**.

It is reasonable to think that the inter-core crosstalk will be lower as long as the core-to-core distance is increased. In contrast, the best way to improve the spatial capacity of the MCF is to increase the core density –number of cores per fiber cross-sectional area– while preserving the capacity of each core. One of the most efficient ways to enhance the mentioned core density is to reduce the core pitch (i.e., the core-to-core distance). However, when shortening the core-to-core distance the inter-core crosstalk becomes a crucial phenomenon and it should be maintained low enough to guarantee the independence of the data sent over the individual cores. Because of this, the inter-core crosstalk characterization and suppression has acquired lot of attention in the research activity over last years.

The inter-core crosstalk has been widely studied during years, and several formulations based on the coupled mode theory (CMT) and the coupled power theory (CPT) have been proposed, [20].

By the analysis of those formulations, it was concluded that the inter-core crosstalk is strongly dependent on the difference between the propagation constants of the involved cores and also on the coupling coefficient between them. The coupling coefficient is related on how much confined is the mode into the cores, so it does not depend on which kind of MCF is used, while the value of the propagation constant of each core is fully-related on which type of MCF is employed. In homogeneous MCFs, since all of the cores have the same propagation constant, the phase-matching condition between cores (i.e. when $\Delta\beta_{mn} = \beta_m - \beta_n = 0$, where β_n represents the propagation constant of the core n) is satisfied and, therefore, higher inter-core crosstalk values are usually obtained. The number of cores that can be multiplexed into the fiber is basically determined by the core-to-core distance for a fixed outer cladding which guarantees a required crosstalk level along a given propagation length. However, since the core-pitch has to be decreased in order to increase the core density, homogeneous MCFs do not support high core packing that exploit the full-capacity of a multicore fiber. To solve this limitation, heterogeneous MCFs were later proposed, where the non-identical cores that compose those MCFs cause a drastic reduction in the power transferred between the cores because a slight difference in effective refractive indices n_{eff} induces a large difference in the propagation constant and the phase-matching condition between cores is avoided (i.e. $\Delta\beta_{mn} = \beta_m - \beta_n \neq 0$), resulting in much lower crosstalk levels than homogeneous MCFs.

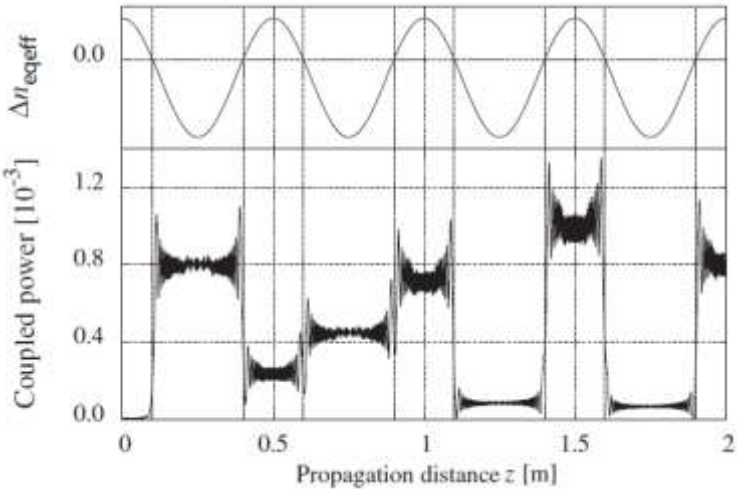

Fig. 2. Example of longitudinal evolution of coupled power in a bent and twisted MCF, [21].

The previous conditions are satisfied when no perturbations are considered, that is, when fiber bends, fiber twists and random structural fluctuations of the fiber are not considered. However, it was found that these perturbations are not negligible in real MCFs and fluctuated along the longitudinal direction of the fiber, and the crosstalk in actual MCFs cannot be predicted without considering them. As an illustrative example, Fig. 2 shows the longitudinal evolution of coupled power in a bent and twisted MCF, extracted from [21]. As it can be appreciated, bend-induced resonant couplings are observed at every phase matching point where the difference between n_{eqeff} (which is the effective index including bending effects) of the cores is equal to zero.

II.2. *EFFECTS OF FIBER BENDS*

As it has been introduced during the previous section, real fiber links can be affected by bends, twists and structural fluctuations of the optical fiber. Those perturbations are not negligible and can strongly affect the resulting crosstalk in MCFs. As shown in Figs. 3(a) and 3(b), bend, twist and structure fluctuation can induce a slight perturbation in the propagation constant of a given core, which can occur also either in the single-core fiber or in the MCF. However, bends can also induce a relatively large perturbation while considering other core as a reference (i.e., an important variation of the effective index difference between both cores due to bend), as shown in Fig. 3(c), and can strongly improve or deteriorate the inter-core crosstalk depending on which homogeneous or heterogeneous MCF is employed.

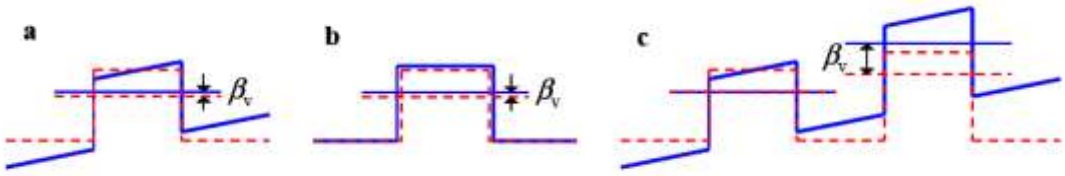

Fig. 3. Schematics of perturbations on the propagation constant, [23]. (a) a slight change of the propagation constant in a core due to bend and twist, (b) a slight change on the propagation constant due to structure fluctuation, and (c) a large bend-induced change on the propagation constant in a core when assuming another core as a reference of the propagation constant.

a) Bent homogeneous multicore optical fiber

Homogeneous MCFs are characterized because all their cores have the same propagation constant (if all the cores are working at the same wavelength). Since curvatures induce a perturbation that change differently the propagation constant of each core, this variation will provide larger reduction of inter-core crosstalk as long as the fiber is curved with smaller bending radius. Fig. 4(b) illustrates the inter-core crosstalk behavior of the homogeneous MCF represented in Fig. 4(a), where it can be appreciated that crosstalk level is reduced when decreasing the bending radius. Therefore, curvatures can be used as a crosstalk suppression technique in homogeneous MCFs.

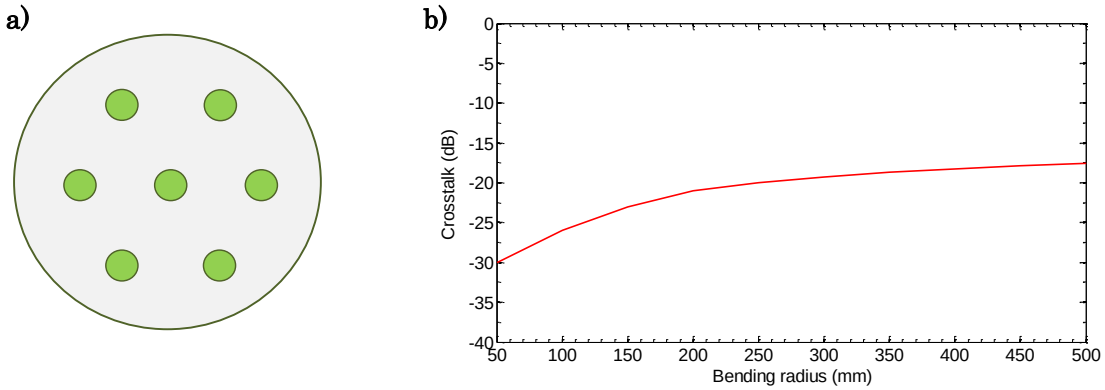

Fig. 4. (a) Schematic cross-section of hexagonal 7-core homogeneous MCF, and (b) illustrative example of the crosstalk versus bending radius behavior in homogeneous MCFs.

b) Bent heterogeneous multicore optical fiber

In heterogeneous MCFs, the behavior is much different than the homogeneous case. Here, the different propagation constants of the cores cause a large crosstalk reduction when the fiber is straight. However, curvatures can produce bend-induced coupling resonances since the propagation constants of two cores can be matched because of bend-perturbations. As shown in Fig. 5, even if two cores have different unperturbed propagation constant, curvatures will perturb it and, for a given bending radius, both cores will be phase-matched. This region is called **phase-matching region**.

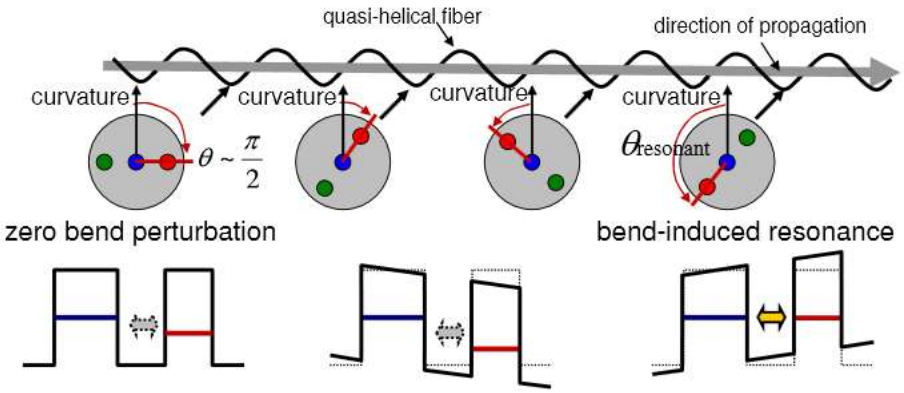

Fig. 5. Schematic of intermittent resonant couplings between two cores at the threshold bending radius as a function of the location of both cores with respect the curvature axis, [24]. Left, zero bend-perturbation; center, perturbation at a given angle between core position-curvature; right, bend-induced resonance.

Consider two particular cores (*m* and *n)* of a heterogeneous MCF. The equivalent effective indices of both cores *m* and *n* are expressed as [17]

$$n_{eqeff,m} = n_{eff,m}\left(1 + \frac{r_m \cos\theta_m}{R_b}\right), \tag{1a}$$

$$n_{eqeff,n} = n_{eff,n}\left(1 + \frac{r_n \cos\theta_n}{R_b}\right). \tag{1b}$$

The phase-matching occurs when the difference $\Delta n_{eqeff} = n_{eqeff,m} - n_{eqeff,n}$ between the equivalent effective indices of two cores equals zero. The bending radius that causes this phase-matching between cores *m* and *n* is the so-called **threshold bending radius** between both cores, $R_{pk,nm}$. If the fiber is bent at this threshold bending radius, the power transferred between cores *m* and *n* will be maximum. In other words, both cores will suffer its maximum inter-core crosstalk. Therefore, by setting to zero the difference between Eq. (1a) and (1b), the threshold bending radius between cores *m* and *n* is

$$R_{pk,mn} = \left|\frac{n_{eff,n}\, r_n \cos\theta_n - n_{eff,m}\, r_m \cos\theta_m}{n_{eff,m} - n_{eff,n}}\right|. \tag{2}$$

Furthermore, we can define a global threshold bending radius given by

$$R_{pk} = \max_{\forall i \neq j}\{R_{pk,ij}\}, \tag{3}$$

which determines the minimum curvature of the fiber to assure non-phase-matching between any pair of cores. Thus, this threshold bending radius should be reduced as much as possible in order to avoid the phase-matching region even if the fiber is curved with small radii. Since the inter-core crosstalk between non-neighbored cores is negligible compared to neighbored cores, the threshold bending radius is only defined between neighbored cores, and therefore, Eq. (3) is simplified so the threshold bending radius between cores i and j may only appear in if both cores are neighbors in the cross-section. The inter-core crosstalk versus bending radius behavior in the 7-core heterogeneous MCF of Fig. 6(a) is shown graphically in Fig. 6(b), where it can be appreciated a peak of maximum crosstalk at a given radius, corresponding to the threshold bending radius.

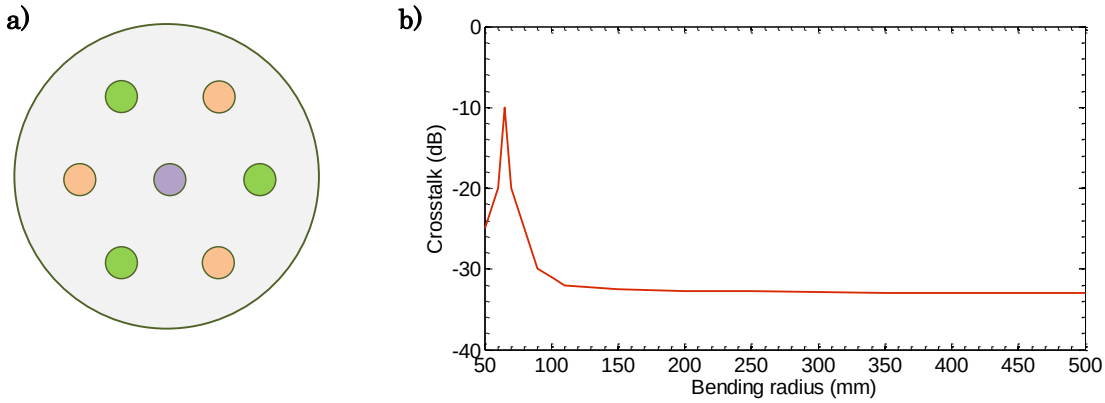

Fig. 6. (a) Schematic cross-section of hexagonal heterogeneous 7-core MCF with 3 kinds of cores, and (b) illustrative example of crosstalk versus bending radius behavior in heterogeneous MCF.

In the particular case of the hexagonal heterogeneous 7-core MCF shown in Fig. 6(a) and by taking the origin of polar coordinates at the midpoint of the cross-section, Eq. (2) can be simplified as

$$R_{pk,mn} = \Lambda \frac{(n_{eff,n} + n_{eff,m})/2}{|n_{eff,m} - n_{eff,n}|}, \tag{4}$$

if any of cores *n* and *m* is the central core, and

$$R_{pk,mn} = \Lambda \frac{n_{eff,n}}{|n_{eff,m} - n_{eff,n}|}, \tag{5}$$

if core *m* is the central core, where Λ is the core pitch. Note that Eq. (4) can be approximated by Eq. (5), since $n_{eff,n}$ and $n_{eff,m}$ are very similar, so Eq. (5) can be either used in both cases. In addition, last expression is also valid for any kind of hexagonal core-distribution with random number of cores (6 cores, 7 cores, 19 cores, etc.). By using Eq. (5), the required effective index difference to shift R_{pk} to the desired value for a given core pitch is illustrated graphically in Fig. 7.

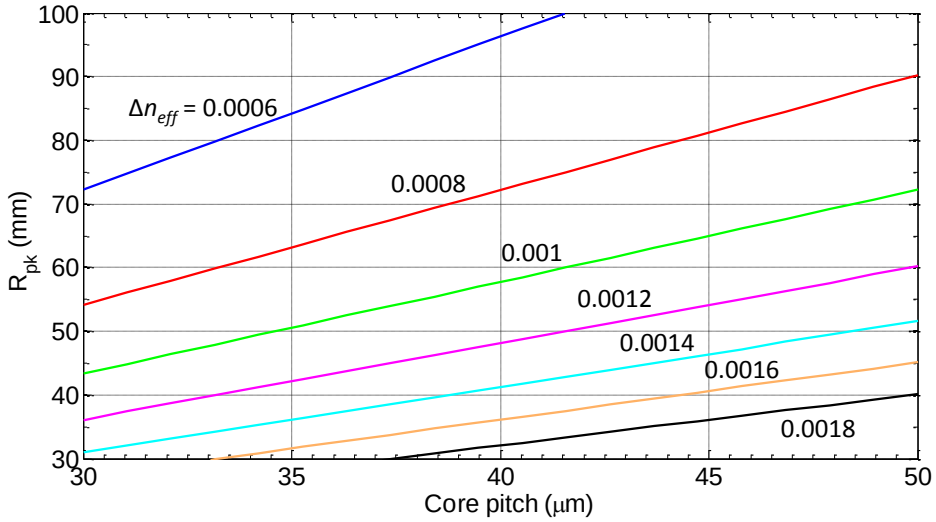

Fig. 7. Relation between effective index difference Δn_{eff} , core pitch and threshold bending radius R_{pk}.

To end with this section, the last important concept related to curvatures in heterogeneous MCF is the so-called **bend-insensitive** MCF, which is a MCF designed to have a threshold bending radius below 50 mm, [15]. This name is received because it is considered physically impossible to do this kind of curvature without breaking the fiber. For instance, as shown in Fig. 7, if one wants to design a bend-insensitive heterogeneous MCF with a core pitch of 35 μm, the effective index difference between any pair of neighbored cores should be larger than 0.001.

II.3. *CROSSTALK SUPPRESSION TECHNIQUES*

Based on the previous concepts studied at this chapter, it can be understood that there are mainly two approaches to crosstalk suppression. One is to decrease the mode-coupling coefficient and the other is to avoid the phase-matching between neighbored cores. Accordingly, there have been proposed various crosstalk suppression methods based on the reduction of those parameters.

The mode coupling coefficient can be suppressed by confining the modes into the cores strongly, increasing the core pitch, and/or using high-index and small-diameter core structures. Since the core-to-core distance is desired to be as short as possible to increase the core density, the first technique is not a viable solution. The method based on high-index and small-diameter core structures degrades the effective area A_{eff} and results in higher fiber non-linearity. Despite those inconvenient, this is an effective and viable method to suppress the crosstalk. The last method is based on the stronger mode confinement, where trench-/hole-assisted MCFs are designed and a large A_{eff} can be preserved. To do this, it is possible to insert trenches or holes surrendering each core, be shared between neighboring cores or even use photonic-crystal structures. Fig. 8 illustrates some of these solutions based on stronger mode confinement.

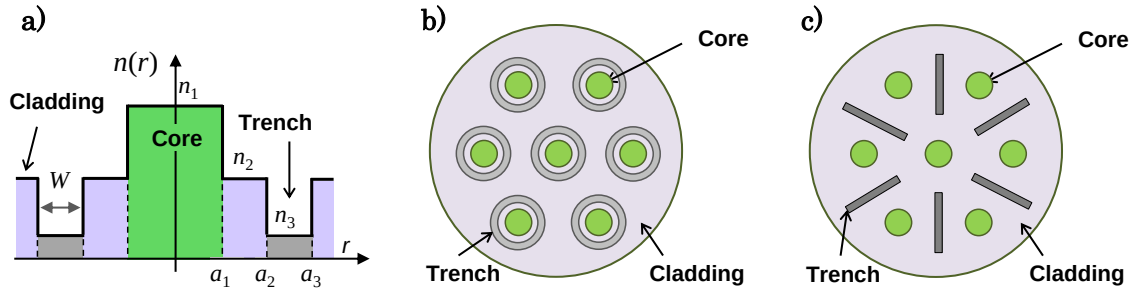

Fig. 8. Schematic examples of (a) trench- assisted refractive index profile, and (b, c) cross-sections of trench-assisted MCFs.

On the other hand, there are several techniques to avoid the phase-matching, like utilizing the propagation constant mismatch, the bend induced perturbation, the longitudinal structural fluctuation and the power spectrum sampling induced by short- and constant-period spin. However, since our proposed TTDLs will be based on heterogeneous MCFs, we will focus on the only technique related to this kind of MCFs, which is the utilization of the propagation constant mismatch $\Delta\beta$ between neighbored cores. Note that the utilization of different propagation constants on each core is the definition of a heterogeneous MCF design. Since all cores will work at the same wavelength, $\Delta\beta$ will be satisfied by using different effective index in neighbored cores. As long as the effective index difference between neighbored cores becomes larger, the crosstalk suppression due to the phase-matching suppression will be higher. To end with this section, it should be noted that all of the last three techniques for avoiding the phase-mating are related to homogeneous MCFs. This can be understood by following a similar process as it was done in the previous section when bent homogeneous MCFs were studied.

III. TRUE-TIME DELAY LINE BASED ON MULTICORE FIBER

III.1. *Theoretical model*

The basic building block of the proposed sampled TTDLs is a single heterogeneous MCF, where each core is designed to have different propagation characteristics. In particular, each core should be designed to have different group delay slope (i.e., different chromatic dispersion parameter, D), and all the cores should also have a common group delay, τ_0, at a given wavelength, λ_0. Hence, by suitable modifications of material and waveguide dispersion, the group delay per unit length of the cores must be tailored according to the incremental law, [13]:

$$\tau_n(\lambda) = \tau_0 + [D_1 + (n-1)\Delta D](\lambda_m - \lambda_0), \tag{6}$$

where $n = 1,2,\dots,N$ is the core number, λ_m is the operation wavelength, D_1 is the chromatic dispersion of core 1, and ΔD is the incremental dispersion parameter between adjacent cores. As it was introduced in the first chapter, if the proposed TTDL is fed by an array of lasers, it offers an

unprecedented 2D operation by exploiting the wavelength and space diversity, as shown in Fig. 9. When operating in space diversity, the basic differential group delay between adjacent cores, for a particular input wavelength λ_m, is given by:

$$\Delta\tau_m(\lambda) = \Delta D(\lambda_m - \lambda_0), \tag{7}$$

where $m = 1,2,\dots,M$ determines the operation wavelength of each laser m. Fig. 10(a) illustrates the space diversity operation. Within a given core n, the use of wavelength diversity yields a basic differential group delay between adjacent wavelengths given by:

$$\tau_n(\lambda) = [D_1 + (n-1)\Delta D]\Delta\lambda, \tag{8}$$

being $\Delta\lambda$ the difference between 2 adjacent input optical wavelength, as shown in Fig. 10(b). Note that if the TTDL is fed by a single optical source, the basic differential group delay between adjacent cores will obey the relation given by Eq. (7), so that the tunability of this 1D-TTDL will be determined by the operation wavelength of the optical source, exploiting only the space diversity.

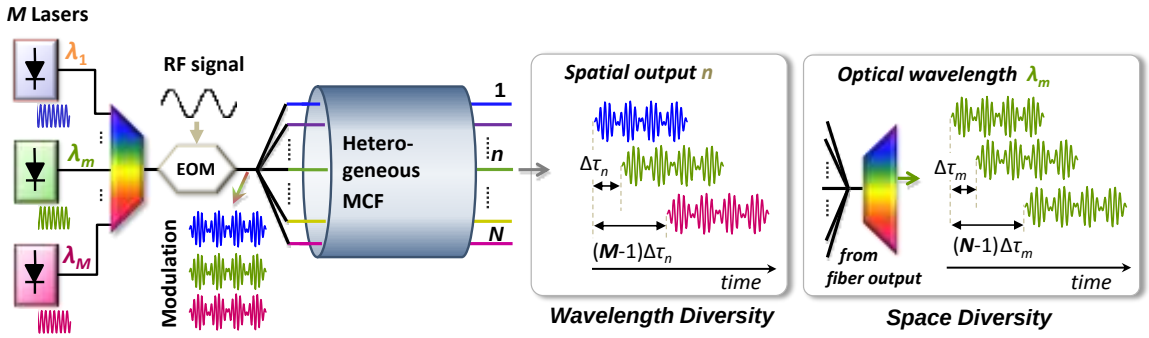

Fig. 9. Schematic of a 2D sampled TTDL fed by a RF modulated multiple optical carriers: illustration of the wavelength and space diversities operation.

In summary, the main goal of the proposed TTDLs will be the appropriated design of the heterogeneous MCF cores that build the TTDL, which must be carried by achieving a common group delay to all of the cores while ensuring at the same time a fixed incremental dispersion between adjacent cores at the reference wavelength. The design and evaluation of both proposed TTDL models are detailed in [26] and [27], respectively.

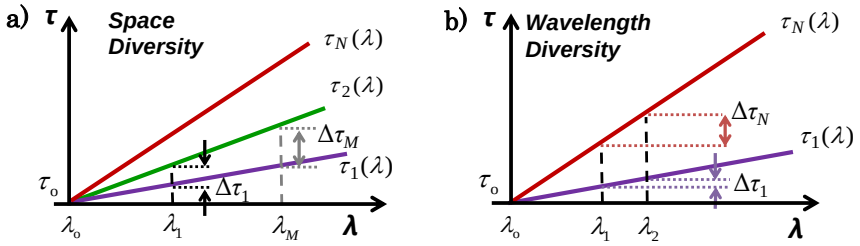

Fig. 10. Graphical representation of 2D TTDL operation: (a) space and (b) wavelength diversities.

III.2. *Design*

The design and evaluation of the heterogeneous MCF used as TTDL will be carried out by means of numerical mode solvers by using the Photon Design software named FIMMWAVE, which includes a large number of rigorous numerical mode solvers that guarantee the most accurate solution to find all the modes of the structure. A full-vector finite-difference method making use of advanced techniques to improve accuracy will be used in the design phase, while a full-vector finite-element method will be used in the evaluation phase.

Considering a negligible inter-core crosstalk, it can be assumed that each core acts as an independent single-mode waveguide transmitting its fundamental mode, so the design of each core of the MCF cross-section can be tailored individually by using a particular single-core single-mode fiber for each of them. The numerical solver provides both the dispersion parameter D and the group refractive index n_g for a particular wavelength. Two different MCF structures have been considered for the TTDL implementation: in the first, each core presents a different refractive step-index (SI) profile surrounded by the cladding; in the second, the refractive index profile of each core is surrounded by its own trench. Both structures are illustrated in Fig. 11, where it can be appreciated the design parameters in each one. Since all the cores must share the same common group delay τ_0, the refractive index profile of each core should be designed so that we obtain the same n_g at the reference wavelength λ_0. In addition, we must assure an incremental value of the dispersion D following the law $D_n = D_1 + (n-1)\Delta D$. In all of the following designs, we consider the same TTDL requirements: 7-sample operation characterized by $\Delta D = 1$ ps/km/nm (i.e., a dispersion range from 1 up to 7 ps/km/nm) at $\lambda_0 = 1520$ nm. Regarding to the MCF characteristics of both models, we consider to build a 7-core MCF with hexagonal core-distribution, where the core-to-core distance is $\Lambda = 35\ \mu m$.

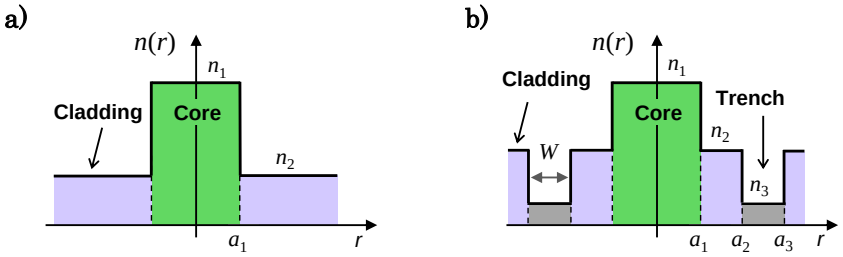

Fig. 11. Schematic of the (a) step-index and (b) trench-assisted step-index profiles of the cores in the first model and in the second, respectively.

a) Model 1: Step-index profile.

As shown in Fig. 11(a), the design of the dispersion profile of the first core model is linked to the selection of two design variables: the core radius a_1, and the fraction of GeO_2 dopant (mol. %) in the SiO_2 core n_1. Hence, in order to find the pair of values $\{a_1, n_1\}$ which satisfy the required group index and chromatic dispersion parameter of each core, as a first step we evaluate the dependence

of the variables n_g and D in an extended range of $2 \leq a_1 \leq 5\ \mu m$ and $1 \leq n_1 \leq 20$ mol. % at $\lambda_0 = 1520\ nm$. We then redefine the range of GeO_2 dopant that offers a set of D parameters wide enough to tailor the required group delay slopes (from Eq. (6)), while assuring a quasi-linear relationship between D and n_1 for each a_1. Particularizing for a 7-core fiber, the selection of a common $n_g = 1.4670$ guarantee the target dispersion ranging from 1 up to 7 ps/km/nm. This is achieved for a GeO_2-dopant concentration bounded between 3.8 and 4.9 mol. %. The selected n_g results in a common group delay per unit length $\tau_0 = n_g(\lambda_0)/c = 4.89\ ns/m$, being c the speed of light in vacuum and $\lambda_0 = 1520\ nm$. Figs. 12(a) and 12(b) show the numerical computation of n_g and D as a function of GeO_2 dopant when a_1 increases gradually from 2 up to 5 μm. As it can be observed, increasing a_1 or n_1 leads on a linear increment of n_g. In the case of the dispersion parameter, if we focus on the desired range of D values which implies $a_1 < 2.7\ \mu m$ and $n_1 > 3.8$ mol. %, increasing the amount of GeO_2-dopant concentration reduces the value of D, but increasing the core radius causes greater D. Note that this reduction will be greater when the core radius is smaller. Attempting to this behavior, it can be concluded that the product $a_1 \times n_1$ should be practically constant for all of the cores in order to satisfy the group index requirements, so the increase of one of this parameters implies a reduction on the other one.

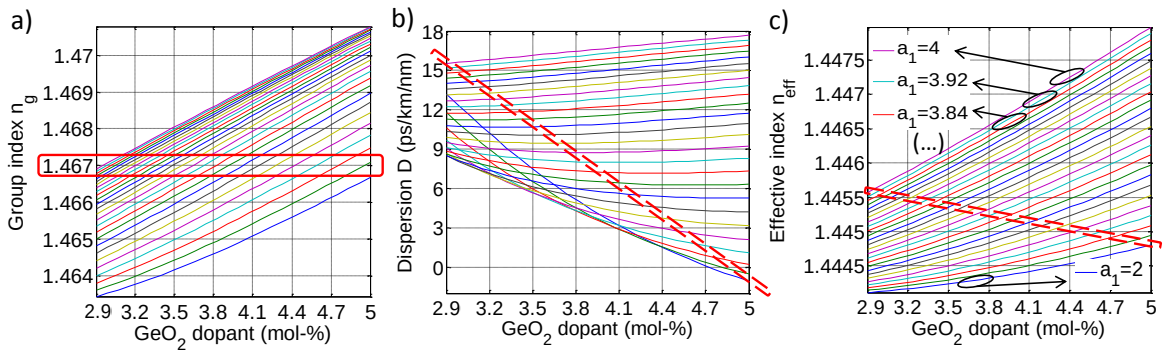

Fig. 12. Group index (a), dispersion (b) and effective index (c) for the SI profile as a function of the core GeO_2 dopant percentage and the core radius.

However, the design of the TTDL is not only subjected to the dispersion profile of the cores, but also by low-crosstalk characteristics. As detailed in section 2.3, the inter-core crosstalk can be easily avoided by increasing the effective index difference Δn_{eff} between neighbored cores, so that it is important to increase this difference as much as possible to improve crosstalk level. Fig. 12(c) shows the dependence of n_{eff} as a function of a_1 and n_1. Note that this behavior is very similar to the group index, so n_{eff} is approximately linearly increasing when a_1 or n_1 grows. As it can be observed, once n_g is fixed to 1.4670, the possible Δn_{eff} values are limited to a range of around 0.0009. Nevertheless, when particularizing for the mentioned 7-core MCF, this range is halved due to the limitation on a_1 and n_1 induced by the desired dispersion range. Therefore, one can observe the impossibility of designing a bend-insensitive MCF with this kind of model, since even between any

2 cores is not possible to reach a Δn_{eff} of around 0.001, which is the minimum value to send R_{pk} between them below 50 mm with the proposed MCF parameters (see Fig. 7).

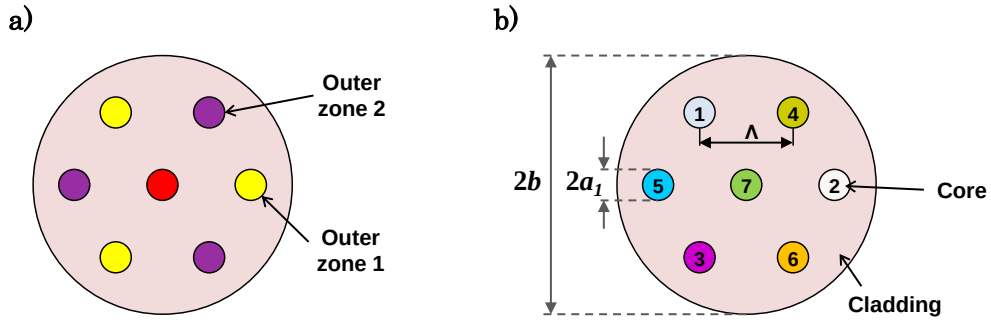

Fig. 13. Schematic cross-section of (a) the different sections is which is divided the MCF (red, yellow and purple), and (b) the final core location of the designed 7-core heterogeneous MCF designed with SI profile.

Taking into account all this considerations, we proceed to design and locate all 7 cores into the MCF. Let's denote cores 1 to 7 at which correspond the dispersion values 1 to 7, respectively. Immediately, one can observe that this first model has not so much versatility because we can only get a single pair of values $\{a_1, n_1\}$ that achieves simultaneously both dispersion and group index particular requirements. Therefore, the effective index is also a fixed parameter for each core n and, as it can be noted by analyzing Fig. 12(b) and (c), it decreases with n, being $n \in \{1,2,..,7\}$ the core number and so the dispersion value of that core. The computed design parameters for this SI profile, which are depicted in rounded markers in Fig. 14, are summarized in Table 1. In order to avoid the phase-matching as much as possible in every pair of neighbored cores, we consider 3 different sections into the MCF cross-section to optimize the location of each core, which are the center core, the outer zone 1 and the outer zone 2, as shown in Fig. 13(a). We then place each core in one of these locations, starting by the center core. We choose core 7 to be located there because it has the highest n_{eff} possible and therefore the mean value of its Δn_{eff} with respect all the other cores is maximized (note that core 1 could also be the central one, since it has the lowest n_{eff}). Then, outer zone 1 and outer zone 2 may have three consecutive cores each one so, since n_{eff} of consecutive core is very similar, we avoid having small Δn_{eff}. For example, we select cores 1 to 3 to be in zone 1, and 4 to 6 in zone 2. We then locate each of those outer cores so that Δn_{eff} is as large as possible between any pair {zone 1, zone 2} of neighbored cores. Fig. 13(b) illustrates the final core-location which minimizes crosstalk.

a) Model 2: Trench-assisted step-index profile.

The second model, based on a trench-assisted (TA) refractive-index profile (as shown in Fig. 11(b)), allows a more versatile design. Apart from the core radius a_1 and the refractive index of the core n_1, the additional design parameters are the inner and the outer radii of the trench, a_2 and a_3. The refractive index of the trench, n_3, can also be changed, but we consider not modifying it for a simple reason: our refractive index profile of the TA-SI model is based on using different GeO_2-

dopant percentage in each section, which means increasing the core dopant to around 12 mol-% and also add some fixed GeO_2-dopant to the cladding (5 mol. %) in order to achieve the required refractive index decrease in the trench (n_3) with respect to the cladding (n_2). Therefore, we consider building the trench by using pure silica with the aim of maximizing the cladding-to-trench index difference and thus improve the trench effect. This low-index trench could also be implemented by using fluorine dopant (usually from 1 to 2 mol. %), [28], which would allow a non-doped cladding and also a less-doped core. Upcoming designs will include this dopant instead of those completely GeO_2-doped designs, but a broad analysis of its behavior will be necessary before using it.

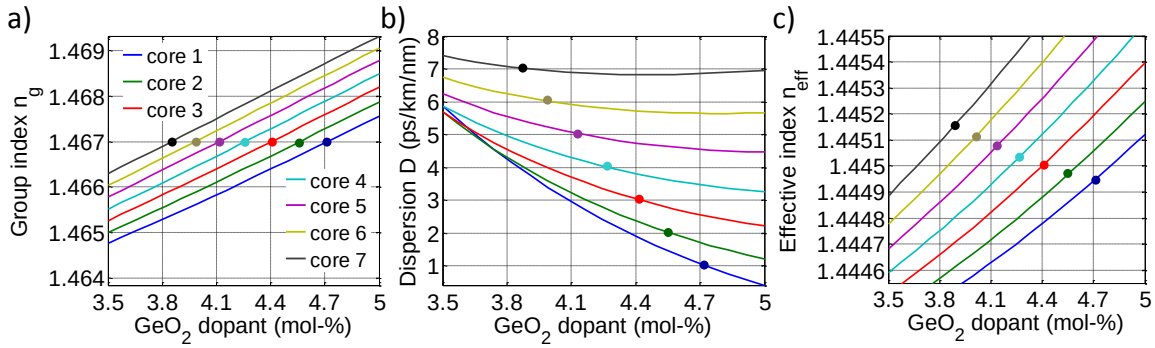

Fig 14. Computed group index n_g (a), dispersion D (b) and effective index n_{eff} (c) for the SI profile as a function of the core GeO_2 dopant percentage.

Core n	a_1 (μm)	Core GeO_2 (mol-%)	n_{eff}	D (ps/km/nm)	n_g
1	2.180	4.73	1.444960	1.00	1.4670
2	2.250	4.56	1.444974	2.00	1.4670
3	2.330	4.42	1.445012	3.00	1.4670
4	2.410	4.27	1.445036	4.00	1.4670
5	2.500	4.15	1.445086	5.00	1.4670
6	2.590	4.00	1.445106	6.00	1.4670
7	2.690	3.90	1.445165	7.00	1.4670

Table 1: Design parameters of each core and its computed values of D, n_g and n_{eff} in the SI profile.

In a similar way than in the first model, we first evaluated the response of n_g, D and n_{eff} while varying all four design parameters. In order to allow a 3D representation of the corresponding simulations, we divide the problem in two parts. First, we analyze these responses when varying the core properties as $2 \leq a_1 \leq 4\ \mu m$ and the GeO_2 dopant between 0.1 and 0.15 mol-%, while letting a_2 and a_3 with fixed values, being $a_2 - a_1 = 5\ \mu m$ and $a_3 - a_2 = 2\ \mu m$. Fig. 15 illustrates n_g, D and n_{eff} responses as a function of the core GeO_2-dopant concentration for different core radii. Note that this behavior is almost the same than in the first model, so we will not analyze it in detail again. In second place, we study the opposite situation: we fix a_1 and core GeO_2 dopant to 2.25 μm and 12.5 mol-%, respectively, and we evaluate the mentioned responses when $a_2 - a_1$ and $a_3 - a_2$ are between 2 and 5 μm. Fig. 16 shows the computed responses as a function of the trench width ($a_3 - a_2$) for different core-to-trench distances ($a_2 - a_1$). Analyzing the first simulation, we can observe that a_1 strongly affects to D so that increases its value when a_1 gets larger, while n_1 does

not affect so much to the dispersion. However, if $a_1 < 2.5\ \mu m$, D becomes also strongly dependent on n_1 and increasing n_1 implies a reduction on D when the core GeO_2-dopant is below 13 mol-%. Regarding to n_g and n_{eff}, it can be appreciated that both are nearly linearly increased when any of a_1 or n_1 increase. With respect to the second simulation, it can be observed that a_3-a_2 does not affect to any parameter unless a_2-a_1 is small. It that case, increasing a_3-a_2 leads on a considerable dispersion growth and also a small increment on the group index. The effective index can be considered invariant with a_3-a_2. On the other hand, increasing a_2-a_1 results on a reduction on both D and n_g, but produces an increment on n_{eff}. Both n_g and n_{eff} are weakly affected by a_2-a_1, while D is strongly affected especially when a_2-a_1 is small enough.

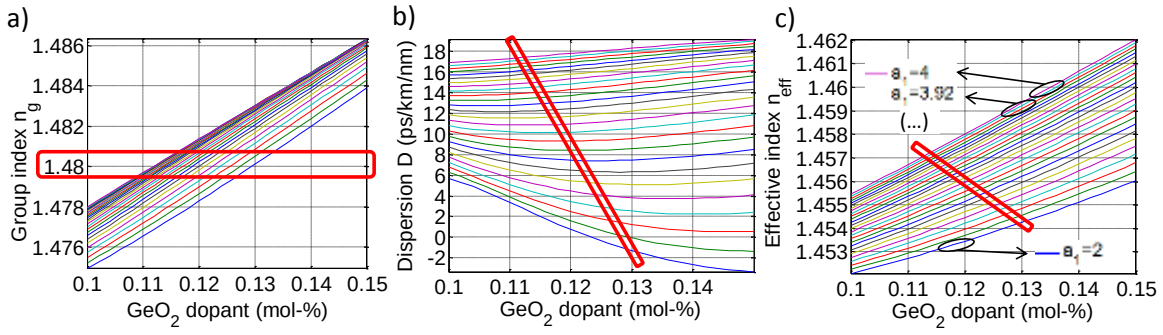

Fig. 15. Group index (a), dispersion (b) and effective index (c) for the TA-SI profile as a function of the core GeO_2 dopant percentage and the core radius, when core-to-trench distance and trench width are fix.

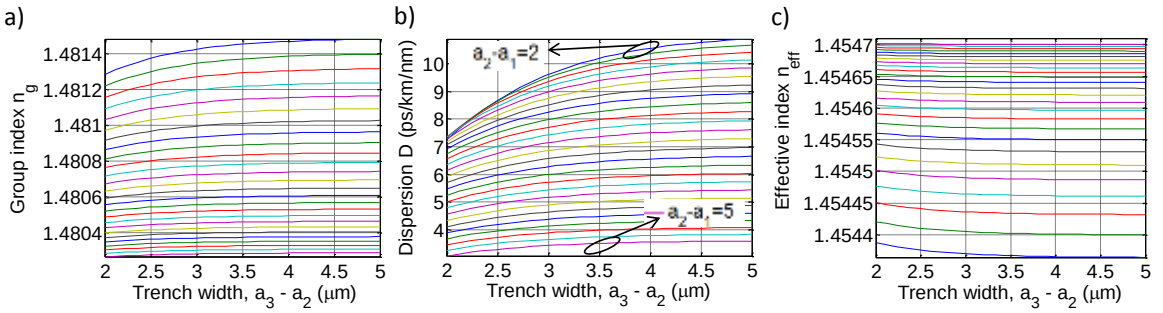

Fig. 16. Group index (a), dispersion (b) and effective index (c) for the TA-SI profile as a function of the core trench width and the core-to-trench distance, when core radius and core GeO_2 dopant percentage are fix.

Taking into account all of the previous considerations and proceeding similarly than in the previous model, we then designed the desired 7-sample TTDL with the TA-SI-profile model with dispersion values from 1 up to 7 ps/km/nm. We have chosen a common group index of 1.4800 for $\lambda_0 = 1520\ nm$ in all of the simulations related to this model, which leads to a common group delay per unit length $\tau_0 = 4.93\ ns/m$. The core design, which involves both a_1 and n_1, plays the most important role in establishing the desired D and n_g. Therefore, we first make a coarse-approximation of the desired D and ng by modifying those parameters and then we refine by also changing the separation and the width of the trench to adjust them. The computed design parameters, which are depicted in rounded markers in Fig. 17, are summarized in Table 2. It can

also be observed the resulting D, n_g and n_{eff} of each core in Table 3, which confirms that the obtained values correspond to the desired ones. Fig. 18 illustrates the final core-location to minimize the inter-core crosstalk. Comparing designs 1 and 2, we can observe that this second design is much better than the first one, since the crosstalk will be reduced not only by the insertion of the trenches, but also because of the increasing on Δn_{eff} between neighbored cores, since the minimum Δn_{eff} between neighbored cores is increased from X to X while using this second model instead of first one.

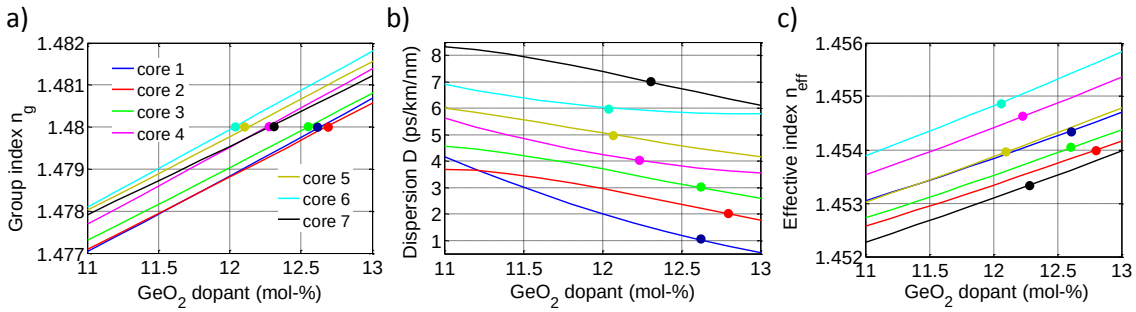

Fig. 17. Computed group index n_g (a), dispersion D (b) and effective index n_{eff} (c) in the second TTDL design (based on the TA-SI-profile model) as a function of the core GeO_2 dopant percentage and the core radius.

Core n	Design 2				Design 3			
	a_1 (μm)	Core GeO_2 (mol-%)	a_2 - a_1 (μm)	$a_3 - a_2$ (μm)	a_1 (μm)	Core GeO_2 (mol-%)	a_2 - a_1 (μm)	$a_3 - a_2$ (μm)
1	2.119	12.63	5.000	2.000	2.000	12.25	2.000	2.088
2	2.004	12.80	3.500	2.000	2.000	12.77	4.190	3.860
3	2.057	12.62	3.500	2.000	2.004	12.74	3.874	4.000
4	2.303	12.26	5.000	2.000	2.057	12.57	3.665	3.000
5	2.160	12.07	3.500	2.000	2.376	12.16	5.000	1.900
6	2.445	12.06	5.000	2.000	2.442	12.06	4.980	2.000
7	2.000	12.30	2.500	4.000	2.521	11.95	5.000	2.000

Table 2: Design parameters of each core and its computed values of D, n_g and n_{eff} in the TA-SI profile.

Core n	Design 2			Design 3		
	D (ps/km/nm)	n_g	n_{eff}	D (ps/km/nm)	n_g	n_{eff}
1	1.00	1.4800	1.454371	1.00	1.4800	1.453173
2	2.00	1.4800	1.453999	2.00	1.4800	1.454012
3	3.00	1.4800	1.454048	3.00	1.4800	1.453978
4	4.00	1.4800	1.454650	4.00	1.4800	1.454015
5	5.00	1.4800	1.453932	5.00	1.4800	1.454780
6	6.00	1.4800	1.454886	6.00	1.4800	1.454877
7	7.00	1.4800	1.453355	7.00	1.4800	1.454992

Table 3: Design parameters of each core and its computed values of D, n_g and n_{eff} in the TA-SI profile.

Despite the mentioned improvements achieved by the previous design, one can observe that it does not involve a rigorous n_{eff} optimization that assures an inter-core crosstalk and threshold bending radius optimizations. Therefore, we have designed a third model by using the same TA-SI profile to illustrate the overall potential of this model. To do this, it is not only necessary to assure

the desired D and n_g values, but also the range of n_{eff} of whole cores must be extended as much as possible, which would cause that Δn_{eff} is increased between every pair of neighbored cores. Furthermore, in a similar manner than it was done in Fig. 13(a), we can optimize the design by considering the same 3 different zones and thus, ensuring that all cores of each zone have a similar n_{eff}, we can maximize the Δn_{eff} between each zone, resulting on a minimization of both the inter-core crosstalk and the threshold bending radius. In order to obtain the minimum n_{eff} zone, it is desirable to have low a_1, n_1 and a_2, but large a_3. Because n_{eff} is mostly dependent on the core parameters, it is reasonable to design the core 1 (i.e. $D = 1\,ps/km/nm$) with this low-effective index, since decreasing a_1 will imply a reduction on the dispersion parameter. Similarly, the high-n_{eff} zone should have high a_1, n_1 and a_2, but this one is independent on the parameter a_3. We select cores 5 to 7 to be in this zone. Therefore, cores 2 to 4 are designed to be in the medium-n_{eff} zone, which can have more randomly values on its parameters.

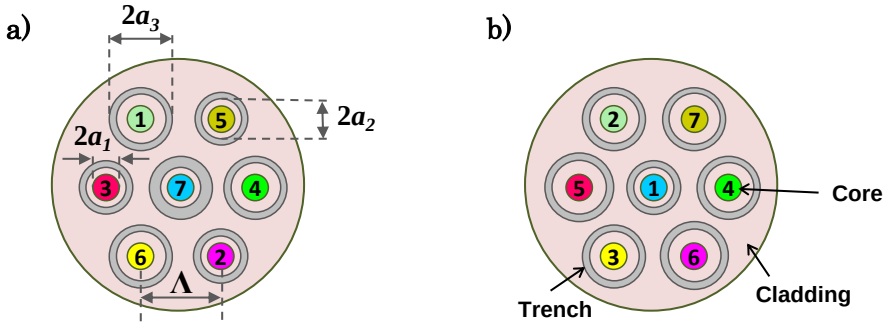

Fig. 18. Core location of both 7-core MCFs built by the TA-SI profile: (a) design 2 and (b) design 3.

Similarly than the previous design, the computed design parameters are depicted in rounded markers in Fig. 19 and summarized in both Tables 2 and 3. The corresponding core location is also illustrated in Fig. 18(b). Attempting to Fig. 19(c), it can be observed that the range of $\Delta n_{eff,max} = n_{eff,max} - n_{eff,min}$ is increased from 0.15% to 0.18% with respect to the previous design and also the design of those 3 different zones with similar n_{eff} allows an effective index difference of around 0.09% between dissimilar zones (i.e., between neighbored cores) instead the worst case of 0.03% obtained in the previous design. Furthermore, the improvement with respect the first design is much higher, since in that case we obtained a range of $\Delta n_{eff,max}$ of around 0.02%.

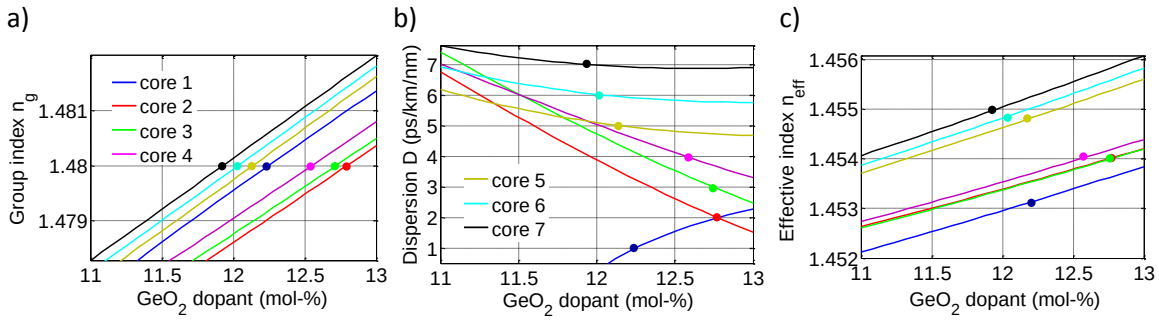

Fig. 19. Computed group index n_g (a), dispersion D (b) and effective index n_{eff} (c) in the third TTDL design (based on the TA-SI-profile model) as a function of the core GeO_2 dopant percentage and the core radius.

III.3. *Evaluation*

Once we have individually tailored the refractive index profile of each core in the two MCF models considered, we can evaluate the group delay dependence on the optical wavelength of the overall TTDL. Since all three designs have the same number of cores and the same incremental dispersion parameter, they feature the same group delay slopes. Those slopes are illustrated graphically in Fig. 20, where the group delay per unit length is represented as a function of the optical wavelength λ calculated from Eq. (6) as the difference $\tau_n(\lambda) - \tau_0$ for a wavelength range up to 1560 nm.

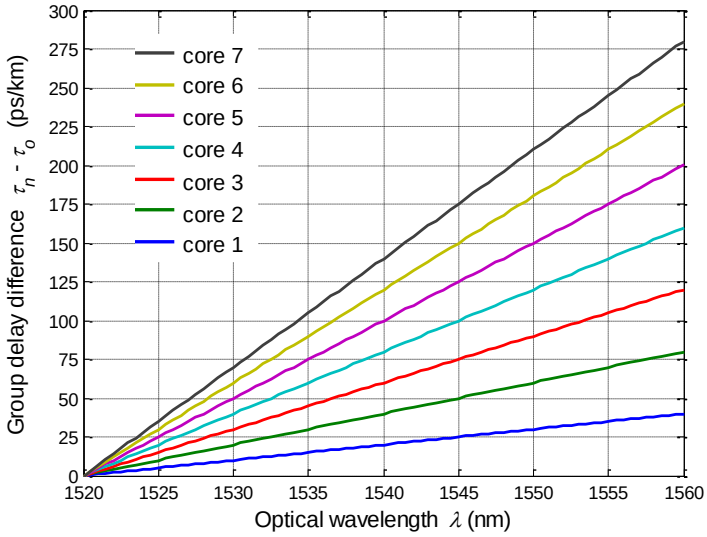

Fig. 20. Group delay difference $\tau_n(\lambda) - \tau_0$ per unit length versus the optical wavelength for each core.

The simultaneous exploitation of the space and wavelength diversity domains in the implemented 2D sampled TTDL adds more versatility as compared to current approaches where only wavelength diversity is exploited [9, 13-14]. If we feed the designed 7-sample TTDLs by an array of M = 10 lasers with $\Delta\lambda$ = 1 nm, we obtain a basic differential delay range spanning from $\Delta\tau_1$ = 1 to $\Delta\tau_7$ = 7 ps/km when exploiting the wavelength diversity [Eq. (8)], while spanning from $\Delta\tau_1$ = 1 to $\Delta\tau_{10}$ = 10 ps/km when using diversity in space [Eq. (7)]. These basic differential delays correspond to the possibility of sampling signal bandwidths ranging from 100 GHz·km to 1 THz·km. For a 10 km MCF, these values yield a record frequency processing range spanning from 10 to 100 GHz, covering part of the X band, the Ku, K, Ka, V bands and part of the W band. Decreasing the MCF length down to 5 km will extend the frequency range from 20 up to 200 GHz, which will also include part of the millimeter band (110-300 GHz). The former bands embrace the vast majority of the present and future MWP applications.

However, as mentioned before, the inter-core crosstalk is one of the major detrimental effects in uncoupled MCF transmissions. Therefore, in this section we will evaluate both crosstalk versus propagation length and crosstalk versus bending radius in order to ensure that crosstalk will be negligible in the first case and also check which will be the threshold bending radius in each design. Note that for the desired propagation lengths crosstalk can be significantly affected by the

fiber bends, so that curvatures become a crucial phenomenon that should be completely characterized for the correct TTDL operation.

First, we evaluate the maximum inter-core crosstalk and the behavior against curvatures of the first design, whose cores were built up by the SI-profile model. Once the core arrangement was optimized to assure that neighbored cores have the highest effective index difference possible [see Fig. 13(b)], the computation of the inter-core crosstalk provided a worst-case value near -40 dB when propagation along a 1-km straight link. As it was commented before, the effective index difference between neighbored cores is quite similar in this first model, featuring a difference $\Delta n_{eff} = n_{eff,n} - n_{eff,m}$ in the range from 0.0059% to 0.0205%. This characteristic will turn more difficult to prevent phase matching conditions between cores and, as a consequence, to reduce the crosstalk. Because of that, we have designed the core radii a_1 small enough to reduce the inter-core mode coupling while keeping the desired dispersion properties. This way we reached worst-case crosstalk levels in the order of those reported for the state-of-art heterogeneous MCFs, [15,16].

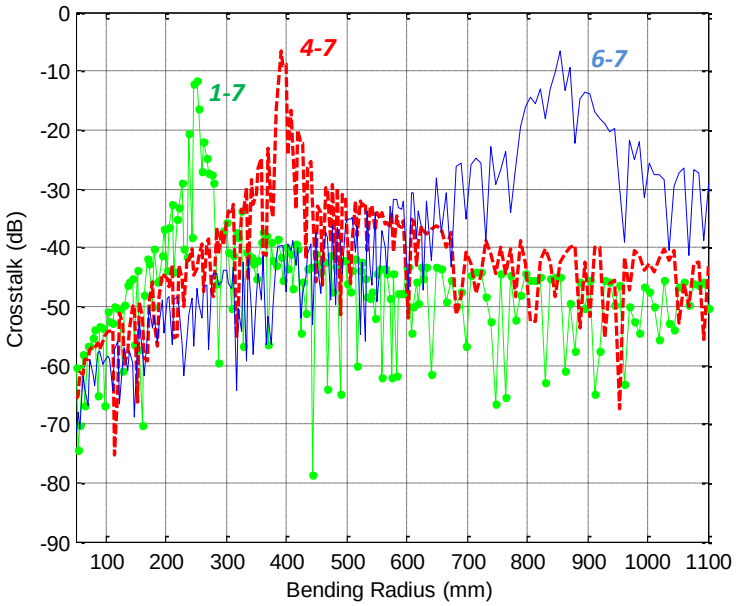

Fig. 21. Computed crosstalk in the SI-profile model as a function of the bending radius. Solid blue line: crosstalk between cores 6 and 7; Red dashed line: crosstalk between cores 4 and 7; Green dotted line: crosstalk between cores 1 and 7.

When evaluating the variation of the crosstalk due to curvatures, the most important parameter is the threshold bending radius. This parameter can be obtained theoretically by using Eq. (4), giving a theoretical worst-case value of $R_{pk} = 857\ mm$ for the designed SI-profile model. Fig. 21 illustrates the computed crosstalk level as a function of the bending radius for three representative cases. In solid blue line we show the worst-case simulation (corresponding to the pair of cores 6-7) where, as expected, a crosstalk peak occurs at the maximum theoretical R_{pk} of 857 mm. As it can be seen, the crosstalk is highly degraded at the vicinities of this threshold value as a consequence of the phase-matching condition between the involved cores. In the non-phase matching region, i.e.

when the bending radius is larger than R_{pk}, the crosstalk level is below -40 dB, which corresponds to the computed crosstalk value when no bends were considered. When increasing the curvature to lower bending radius, different peaks can appear due to the interaction of any pair of cores. Because of this, it is highly desirable to not decrease the bending radius below R_{pk} in order to avoid those high-crosstalk values which can induce large degradations. This behavior is also illustrated in Fig. 21, where we show the crosstalk behavior for two additional pair of cores: cores 4 and 7 in red dashed line, where its R_{pk} is located around 392 mm, and cores 1 and 7 in green dotted line, where its R_{pk} is reduced to approximately 247 mm.

With respect to the TA-SI-profile model, the evaluation of the inter-core crosstalk level for a 1-km link without curvatures provided a large reduction on the worst-case value. For instance, the second design (i.e. the first design of this second model) experiences a drastic reduction of this value down to -100 dB. As compared to the previous model based on the SI-profile, this improvement in the crosstalk performance is due to the reduction of the mode coupling coefficient by the insertion of the trenches, and also to the higher Δn_{eff} between neighbored cores, which ranges from 0.0323% to 0.15%. It should be noted that this design provides a worst-case crosstalk level much lower than the -70 dB reported in the literature for trench-assisted MCFs, [25]. The third design (i.e. the second design of this second model) reaches even lower values than the second one because of the extension of the $\Delta n_{eff,max}$ range and also the optimization on the Δn_{eff} between neighbored cores. In this case, a worst-case crosstalk level close to -110 dB is obtained.

One of the main advantages of the TA-SI-profile model can be further appreciated from the evaluation of the threshold bending radius. By using Eq. (4), a maximum theoretical value of $R_{pk} = 158\,mm$ is obtained in the second design by the interaction of the pair of cores 1 and 3, which is much lower than the 857 mm maximum R_{pk} reached in the first design. Nevertheless, this radius can even be shifted to lower values when using the optimized method, which corresponds to the third of our proposed designs. In this third design, the theoretical threshold bending radius is located at 66 mm, which occurs due to the phase-matching between cores 2 and 5. Fig. 22(a) shows the computed crosstalk in the second design as a function of the bending radius for three representative pairs of cores. The solid blue line corresponds to the worst case, the green dotted line to the pair of cores 1 and 5, and the red dashed line to the cores 3 and 7. In addition, Fig. 22(b) illustrates the computed crosstalk in the third model as a function of the bending radius. Note that in this case we only show the worst-case simulation because the threshold bending radius is close to 50 mm, which is the limit radius considered for all these simulations. As observed with the first model, the maximum power transfer between cores occurs at the worst-case R_{pk} calculated from Eq. (4). For regions above these values, the MCF designed upon trench-assisted core profiles assures a negligible crosstalk value below -100 dB in the second design and below -110 dB in the third one for every pair of cores.

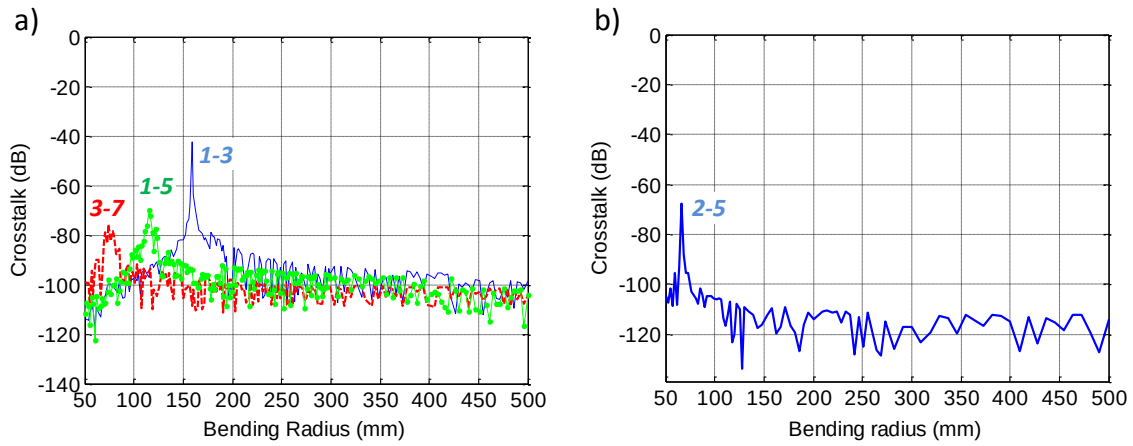

Fig. 22. Computed crosstalk in the TA-SI-profile model as a function of the bending radius. (a) Second design (solid blue line: crosstalk between cores 1 and 3; red dashed line: crosstalk between cores 3 and 7; green dotted line: crosstalk between cores 1 and 5) and (b) third design (crosstalk between cores 2 and 5).

IV. APPLICATION: OPTOELECTRONIC OSCILLATOR

IV.1. *Introduction*

A particularly attractive MWP application is the implementation of optoelectronic oscillators (OEOs). The OEO is fundamentally similar to the van der Pol oscillator replacing the energy-storage function of the LC circuit by a long fiber-optic delay line, complemented with the corresponding I/O optical devices (i.e. laser, modulator and photodetector). Initially proposed by Yao and Maleki [29], single cavity OEOs can provide ultra-stable, tunable and extremely low-linewidth RF frequency generation in a broad frequency range, rivaling the best crystal oscillators. With the aim of generating high spectral-purity signals in single cavity OEOs, a long fiber loop is necessary, but it results in a generation of a considerable number of oscillation modes that force the incorporation of very selective RF filters in the electronic part of the system. To combat this limitation, several solutions have been proposed to refine and improve the performance of OEOs, including the incorporation of a highly selective whispering gallery optical filter in the optical segment of the oscillator that can lead to extremely compact, broadly tunable and low phase noise devices with the possibility of exploiting as well opto-mechanical effects. Coupled optoelectronic oscillators (COEOs), which simultaneously produce spectrally pure microwave signals as in a OEO and short optical pulses as in a mode locked laser, have also been proposed and actively reached during the last years. Finally, multi-cavity or multiloop OEOs have been proposed, where a long cavity provides the required spectral purity and a short fiber cavity provides the required spectral separation between adjacent oscillating modes, alleviating the narrowband requirement for the internal RF filter. Furthermore, these structures can be generalized to an arbitrary number of loops and its design optimized for cavity lengths that are multiple of a given reference value.

In this context, we propose the use of MCFs for the implementation of multi-cavity OEOs. MCF provides an ideal medium for the implementation of multiple parallel cavities, all of which will be subject to practically identical mechanical and environmental conditions. In a first place, we extend the theory developed in [19] for the case of two cavity OEOs to a general number *N* of cavities providing the equations describing the oscillation spectrum, amplitude and phase oscillation conditions, and phase noise spectrum. Then, we describe the proposed configurations based on both homogeneous and heterogeneous MCFs. In practical terms, the required MCFs feature lengths ranging from a few meters to < 10 km. For this lengths, the inter-core crosstalk can be easily decreased below < -40 dB, as it was demonstrated in the previous chapter, which will have a negligible impact on the independent cavity operation.

IV.2. *Multi-cavity OEO model*

a) *Signal*

Fig. 23 shows the general layout of the proposed multi-cavity OEO. A common optical source, modulator, RF amplifier, photodetector and RF filter are shared by the different cavities. Considering that the RF filter has a sufficiently narrow bandwidth to block all harmonic components, the output of the global device is related with the input voltage as:

$$V_{out}(t) = G(V_o)\, V_{in}(t), \tag{9}$$

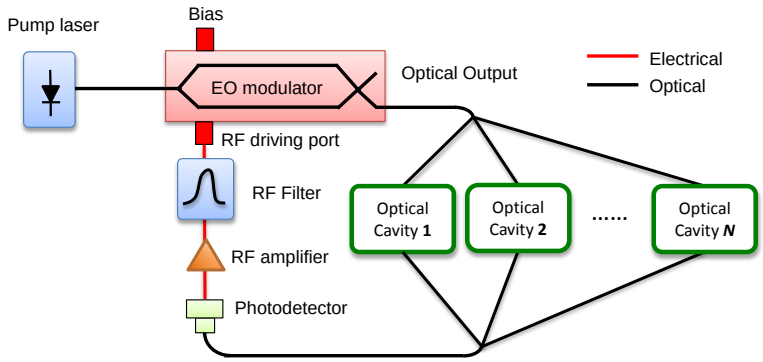

Fig. 23. Layout of a multi-cavity optoelectronic oscillator.

where $G(V_o)$ is the voltage-gain coefficient. In general, $G(V_o)$ is a function of the frequency ω of the input signal due to the effect of the amplifier and the photodetectors. Therefore, we can divide this parameter in two parts: one independent on the frequency, $G(V_o)$, and another frequency dependent, $H(\omega)$. Moreover, since each cavity is implemented in the optical domain using different cores of a single MCF and features a different round-trip complex-value gain g_k given by

$$|g_k| = G_k |H_k(\omega)|, \tag{10a}$$

$$\phi_k = \arg[H_k(\omega)], \tag{10b}$$

where G_k is the voltage gain coefficient of loop k and $\tilde{H}_k(\omega) = |H_k(\omega)| \exp(j\phi_k)$ the unitless complex filter function that accounts for the combined effect of all frequency dependent components in the cavity k, Eq. (9) can be rewritten as:

$$\tilde{V}_{out}(t) = \tilde{V}_{in}(\omega, t) \sum_{k=1}^{N} G_k(V_o)\, \tilde{H}_k(\omega) = \tilde{V}_{in}(\omega, t) \sum_{k=1}^{N} |g_k|\, e^{j(\omega\tau_k + \phi_k)}, \tag{11}$$

being $\tilde{V}_{in}(\omega, t)$ and $\tilde{V}_{out}(t)$ the complex input and output voltages, respectively.

It should be remarked that our proposal, [30], can be considered an extension of earlier reported systems for three reasons. In first place, as we will see, it allows not only for the implementation of multiple cavity OEOs where cavity lengths are a multiple of a given reference value, as proposed in [31], but also of multiple cavity OEOs where cavity lengths are slightly different exploiting the Vernier effect. In second place, the use of a single multicore fiber structure to host all the cavities provides an integrated hosting medium for enhancing their relative stability against environmental fluctuations. Finally, if properly designed heterogeneous MCFs are employed (see chapter 3), then tunable multiloop OEOs can be potentially implemented.

Once the input signal is in the oscillator, it will circulate in the loops, and the recursive relationship for the complex amplitude of the circulating fields of Eq. (11) after the r^{-th} round-trip can be expressed following a similar procedure as Yao and Maleki, [29], as:

$$\tilde{V}_r(\omega) = \tilde{V}_{r-1}(\omega) \sum_{k=1}^{N} |g_k|\, e^{j(\omega\tau_k + \phi_k)}. \tag{12}$$

Hence, if the oscillation starting voltage is given by $G_a\tilde{V}_{in}(\omega)$, where G_a is the RF amplifier voltage gain, then the application of Eq. (12) yields:

$$\tilde{V}_{out}(t) = \sum_{r=0}^{\infty} \tilde{V}_r(\omega) = \frac{G_a\tilde{V}_{in}(\omega)}{1 - \sum_{k=1}^{N} |g_k|\, e^{j(\omega\tau_k + \phi_k)}}, \tag{13}$$

and the corresponding RF power:

$$P(\omega) = \frac{\left|\tilde{V}_{out}(\omega)\right|^2}{2R} = \frac{G_a^2 \left|\tilde{V}_{in}(\omega)\right|^2 / 2R}{1 + \sum_{k=1}^{N} |g_k|^2 + 2\sum_{\substack{k=1 \\ l>k}}^{N} |g_k||g_l| \cos[\Phi_k(\omega) - \Phi_l(\omega)] - 2\sum_{k=1}^{N} |g_k| \cos[\Phi_k(\omega)]}, \tag{14}$$

where R is the load impedance of the RF amplifier and:

$$\Phi_k(\omega) = \omega\tau_k + \phi_k. \tag{15}$$

For oscillations to start collectively in all the cavities at an angular frequency ω_0 we need:

$$\Phi_k(\omega_0) = 2m_k\pi, \tag{16a}$$

$$\Phi_k(\omega_0) - \Phi_l(\omega_0) = 2(m_k - m_l)\pi, \qquad m_k, m_l \in Z. \tag{16b}$$

Under these conditions, then:

$$P(\omega_0) = \frac{G_a^2 \left|\tilde{V}_{in}(\omega_0)\right|^2 / 2R}{1 + \sum_{k=1}^{N} |g_k|^2 + 2\sum_{\substack{k=1 \\ l>k}}^{N} |g_k||g_l| - 2\sum_{k=1}^{N} |g_k|}. \tag{17}$$

In order for the oscillation to start from noise, the denominator in Eq. (17) must vanish:

$$1 + \sum_{k=1}^{N} |g_k|^2 + 2\sum_{\substack{k=1 \\ l>k}}^{N} |g_k||g_l| - 2\sum_{k=1}^{N} |g_k| = 0. \tag{18}$$

A simple case is when the gain coefficients have equal moduli in all cavities $|g_k| = g, \ \forall k$, in which case, Eq. (18) leads to:

$$|g| = 1/N. \tag{19}$$

b) *Spectrum*

The spectrum of the oscillating signal can be computed by determining the power spectral density of noise in the oscillator. Following again a similar procedure as Yao and Maleki illustrated in [32], we have:

$$\rho_N(\omega)\Delta f = \frac{\left|\tilde{V}_{in}(\omega)\right|^2}{2R}, \tag{20}$$

where Δf is the frequency bandwidth and $\rho_N(\omega)$ the power density of the input noise at frequency ω. Here, $\rho_N(\omega)$ takes into account all the technical noise sources in the OEO, including thermal, shot, relative intensity noise and, when applicable, amplified spontaneous emission noise, [29]. Substituting Eq. (20) into Eq. (14) and taking Eq. (15) and Eq. (16) into consideration, we find the following expression for the power spectral density of the oscillating mode at ω_0:

$$S_{RF}(f') \equiv \frac{P(f')}{\Delta f P_{osc}} = \frac{G_a^2 \rho_N / P_{osc}}{1 + \sum_{k=1}^{N} |g_k|^2 + 2\sum_{\substack{k=1 \\ l>k}}^{N} |g_k||g_l| \cos[2\pi f'(\tau_k - \tau_l)] - 2\sum_{k=1}^{N} |g_k| \cos[2\pi f' \tau_k]}, \tag{21}$$

where $f' \equiv \frac{\omega - \omega_0}{2\pi}$ is the frequency offset from the RF carrier and P_{osc} represents the RF oscillation power. Taking into account that the argument of the cosines in Eq. (21) would have small values for reasonable frequency offsets, we can approximate all of the cosines for their corresponding Taylor series as:

$$\cos(\Phi_k - \Phi_l) = \cos\big(2\pi f'(\tau_k - \tau_l)\big) \approx 1 - \frac{\big(2\pi f'(\tau_k - \tau_l)\big)^2}{2}, \tag{22a}$$

$$\cos(\Phi_k) = \cos(2\pi f' \tau_k) \approx 1 - \frac{(2\pi f' \tau_k)^2}{2}, \tag{22b}$$

where we use the approximation $\cos(x) \approx 1 - \frac{x^2}{2}$, if $x \downarrow\downarrow$.

From Eq. (21), Eq. (22a) and Eq. (22b), it can be concluded that, for a fixed frequency offset, the phase noise of the OEO will decrease when the time delay of the cavities increases. Therefore, it is desirable to have longer cavities (i.e. cavities that induce larger time-delays) in order to have lower phase noise. However, as we will see later, short cavities are needed to increase the spectral separation between adjacent oscillating modes. Because of that, mixed configurations with long- and short-cavities or vernier configurations where all cavities have long-lengths and very similar time-delays are required with the aim of exploiting both advantages.

IV.3. *Multi-cavity OEOs using homogeneous multicore fibers*

The identical multiple cores of a homogeneous MCF can be employed to implement both double- and multiple-cavity OEOs. As we exposed in the second chapter, this kind of MCFs can experience inter-core crosstalk issues, since the phase-matching is not prevented between neighbored cores. However, treating adequately the core-profile design (i.e. using trench-assisted configurations) and the core pitch, this problem can almost be avoided at least for short-length transmissions. Taking into consideration, as we will see, that MCF lengths required for OEOs range in between a few meters and a few km, it is expected that inter-core crosstalk will have a negligible impact.

a) *Double unbalanced cavity OEOs*

Fig. 24(a) shows the layout of a double-cavity OEO based on an N-core homogeneous MCF. Here, k_1 ($k_1 < N/2$) cores are linked to form the first (short) cavity while remaining N-k_1 cores form the second (long) cavity. If the core lengths are all equal to L and the group delay per unit length is given by τ_{g0}, then each core provides a group delay given by $\tau = \tau_{g0}L$. In this first model, the oscillation frequency must verify:

$$f_0 = \frac{m}{k_1 \tau_{g0} L}, \qquad m = 1,2,\dots \ , \tag{23a}$$

$$f_0 = \frac{n}{(N-k_1)\tau_{g0} L}, \quad n = 1,2,\dots \ . \tag{23b}$$

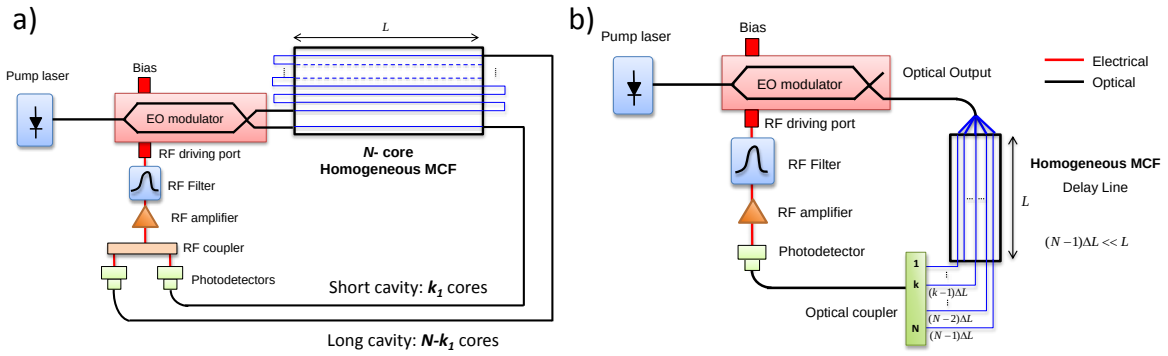

Fig. 24. (a) Double unbalanced cavity OEO using an N-core homogeneous MCF, and (b) multiple-cavity OEO with almost equal length (vernier OEO).

As it was introduced before, Eq. (23a) indicates that the spectral separation of the oscillating modes will be determined by the length (or time delay) of the short cavity, being larger when this length is smaller. Therefore, Eq. (23a) is employed to determine the required value of L, taking as a starting point the knowledge of f_0, N, k_1, τ_{g0} and a set value for m. Once the value of L is set, we then obtain the value of n from Eq. (23b). For example, for an oscillation frequency of f_0 = 10 GHz and a typical 7-core MCF (N = 7), if k_1 = 1 and τ_{g0} = 5 ns/m, setting m = 100 yields L = 2 m and n = 600, leading to a short cavity of 2 m and a long cavity of 12 m. The oscillation spectra of this case is shown in Fig. 25(c), where an RF filter centered at 10 GHz and with maximum bandwidth of 100 MHz is enough for single-mode oscillation. In addition, Fig. 25(a) and Fig. 25(b) illustrate how the short-loop and the long-loop cannot oscillate by its own in isolation. It can also be appreciated that the short loop determines the oscillation-spectra periodicity, as commented.

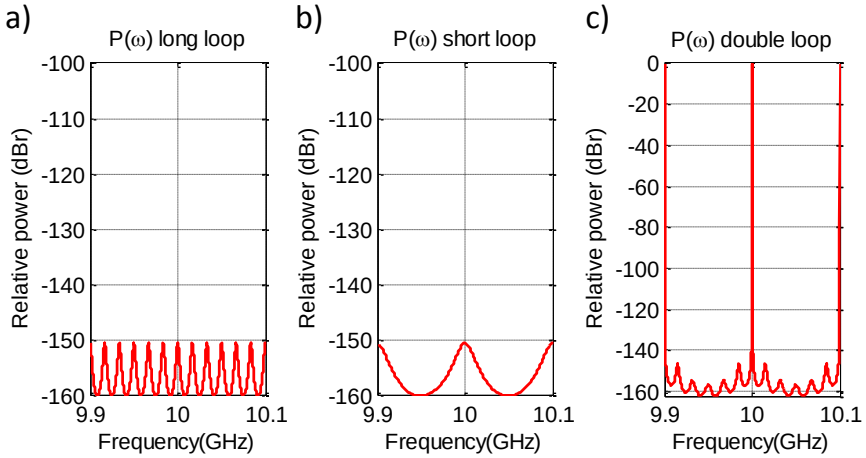

Fig. 25. Oscillation spectra for a double unbalanced cavity OEO using a 2-meter 7-core homogeneous MCF as a delay cavity, where long cavity is formed by using 6 cores (12 m) and short cavity by a single core (2 m). (a) Long loop alone closed, (b) short loop alone closed, and (c) both loops together closed.

If we change the number of cores that forms each loop by setting k_1 = 2 or 3, a short cavity of 4 m and a long cavity of 10 m is obtained in the first case, and a short cavity of 6 m and a long one of 8 m in the second. A priori, one can think that the free spectral range of the OEO will be shorter since the short cavity-length is increased. However, in this case the spectral periodicity will be the same because the oscillation frequencies supported simultaneously by both cavities in isolation are exactly the same than the case of k_1 = 1. This can be understood by analyzing Eq. (23a) and Eq. (23b). When k_1 = 1, the oscillation spectra periodicity is proportional to $1/L$ and $1/(6L)$. Since $1/L$ is a multiple of $1/(6L)$, the oscillation frequencies of the short cavity will be included into the oscillation frequencies of the long one, so that the oscillation frequencies of the global OEO are exactly the same than the short cavity oscillation frequencies. However, this will not happen when $k_1 \neq 1$. For example, in the case of k_1 = 2,in the short cavity we have frequencies located in multiples of $1/(2L)$, while in the long one in multiples of $1/(5L)$. Hence, the oscillation frequencies of the OEO will not be exactly the same than the short cavity frequencies. A similar behavior

happens when k_1 = 3. In order to explain graphically this behavior, Fig. 26(a-c) shows the oscillations frequencies of the OEO when k_1 = 2.

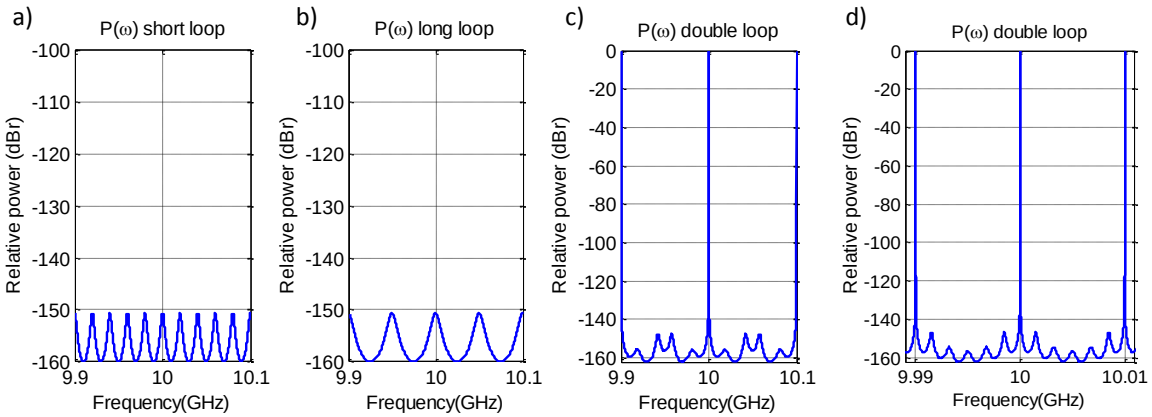

Fig. 26. Oscillation spectra for a double unbalanced cavity OEO using a 2-meter 7-core homogeneous MCF as a delay cavity for (a), (b) and (c) with k_1 = 2, and a 20-meter MCF as a delay cavity for (d) with k_1 = 1.

The computed results for the OEO phase noise spectra are shown in Fig. 27. In order to illustrate how the phase noise is improved when the long-cavity length is increased, we also compute the OEO phase noise spectra when the length of the MCF is fixed to L = 20 m. That results in a short cavity of 20 m and a long cavity of 120 m for k_1 = 1, reaching a 20 dB reduction on the phase noise spectra. However, the increment on the short cavity length results in a requirement of an RF filter with a 10 MHz bandwidth instead the 100 MHz bandwidth of the previous case, as shown if Fig. 26(d). Note that changing the number of cores that form the long cavity yields on a slight different responses, but the difference will be mostly negligible in terms of phase noise with respect the case k_1 = 1, especially for lower offset frequencies.

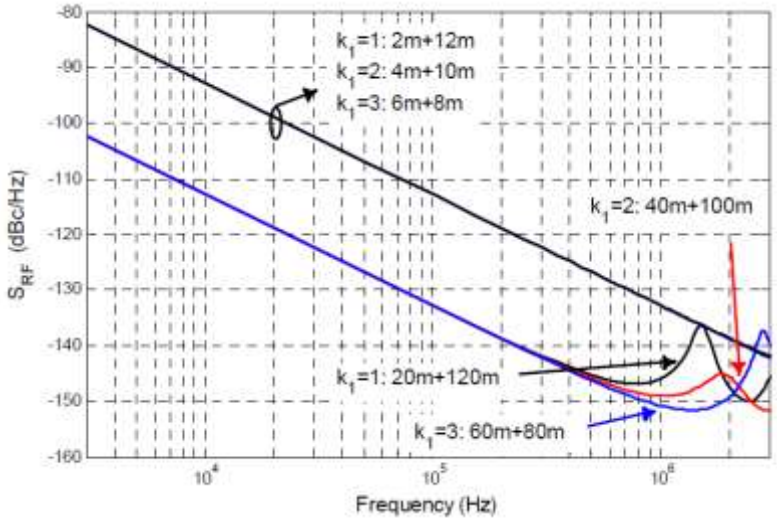

Fig. 27. (Upper trace) Phase noise spectra computed for the cases of Fig. 25 and Fig. 26. (Lower trace) Phase noise spectra computed for the same situations but when L = 20 m. Standard noise (ρ_N = -180 dBm/Hz), RF gain (Ga = 10) and oscillation power (P_{osc} = 16 dBm) values have been employed.

In order to improve this model in terms of oscillation spectral periodicity and also in the phase noise response, we can increase the length-difference between the short- and long cavities by employing a 19-core MCF, where 1 core can be used as short cavity and the remaining 18 to build up the long one.

b) *Multi-cavity vernier OEOs*

Fig. 24(b) shows the layout for a multiple cavity OEO where the different cores of the MCF are employed to build cavities with slightly different physical length. Here, the homogeneous MCF with core length L is coupled to an output photonic lantern with different (but even spaced by ΔL) physical lengths in its output ports. This photonic lantern features in consequence incremental delays between adjacent ports given by $\Delta\tau = \tau_{g0}\Delta L$. In this case, Eq. (15) results:

$$\Phi_k(\omega) = \omega\tau_{g0}L + (k-1)\omega\tau_{g0}\Delta L + \phi_k \qquad for\ k = 1,2,\dots,N. \tag{24}$$

Assuming $\phi_k = 0\ \ \forall k$, the oscillation frequency must verify:

$$f_0 = \frac{m}{\tau_{g0}L}, \tag{25}$$

which is employed to determine the required value of L taking as a starting point the knowledge of f_0, τ_{g0}, and a set value for m. For the rest of the cavities, in order to have vernier effect [33] operation and constructive interference at f_0, we require:

$$2\pi f_0\Delta\tau = 2\pi \quad \rightarrow \quad f_0 = \frac{1}{\tau_{g0}\Delta L}. \tag{26}$$

From Eq. (25) and Eq. (26) we have $L/\Delta L = m$. Hence, although the free spectral range of each cavity is approximately $1/\tau$, the free spectral range value of the coupled-cavity configuration is $1/\Delta\tau = m/\tau$ due to the vernier effect. For example, for an oscillation frequency f_0 = 10 GHz and a MCF featuring τ_{g0} = 5 ns/m setting m = 1000 yields L = 20m and ΔL = 2cm, which is an incremental value that can be easily achieved in a compact photonic lantern device closing the MCF. Fig. 28 shows the oscillation spectra for this example when the number of cavities ranges from 2 up to 7.

Note that, in this case, the overall coupled cavity free spectral range is 10 GHz, despite the fact that the free spectral range values for the individual cavities are around 10 MHz, so the mode selection does not require a selective RF filter. In addition, it can be noted that increasing the number of cavities leads on a reduction of the oscillation linewidth and also on a better rejection of the spurious modes generated in this OEO configuration.

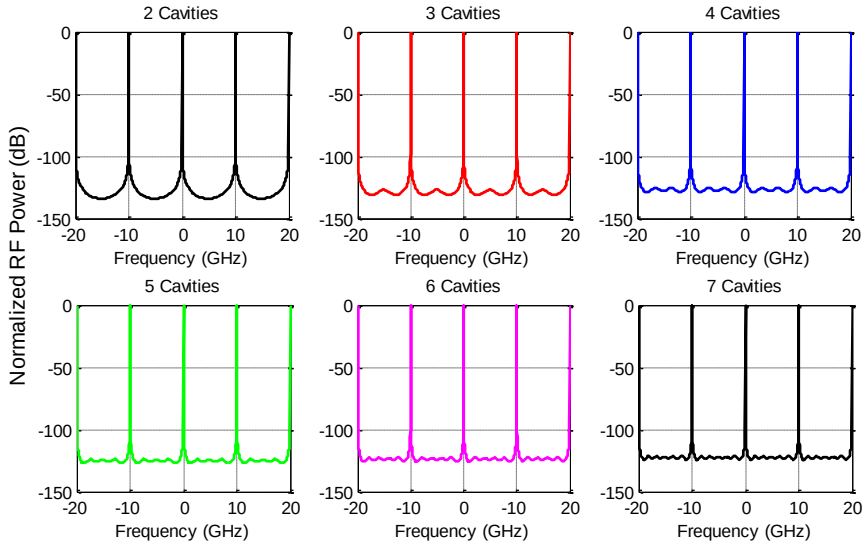

Fig. 28. Oscillation spectra for a multi-cavity vernier OEO using a 20-meter 7-core homogeneous MCF.

Since all cavities have very similar lengths, the propagation delay of each cavity will be mostly equal, so that the difference between having 2 or 7 cavities will be negligible in terms of linewidth, being their phase noise spectra practically the same. For example, Fig. 29 shows the phase noise spectra for the case of 7 cavities (red) and for the case of 2 cavities (blue), where the short cavity has a length of 100 m in both cases, and the following cavities have an increment of 0.02 m compared to its predecessor. As it can be appreciated, both lines are overlapped, confirming the similarity between the spectra in both cases.

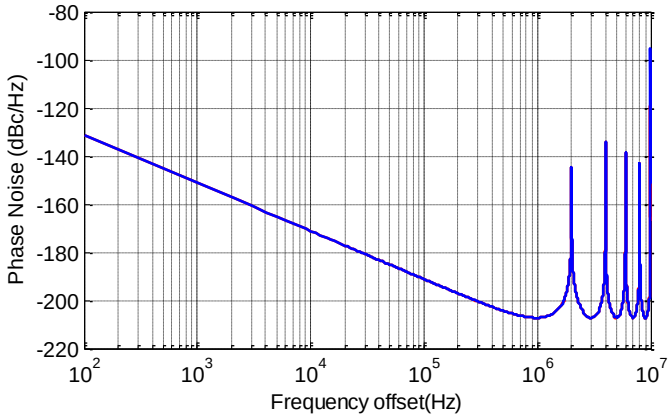

Fig. 29. Phase noise spectra computed for a multi-cavity vernier OEO using a homogeneous MCF.

IV.4. *Multi-cavity OEOs using heterogeneous multicore fibers*

Heterogeneous MCFs can also be employed to implement tunable multi-cavity OEOs. In this case, the cores of the MCF should be designed to create a TTDL by following the design procedure detailed in the previous chapter. The basic layout of the proposed OEO is shown in Fig. 30.

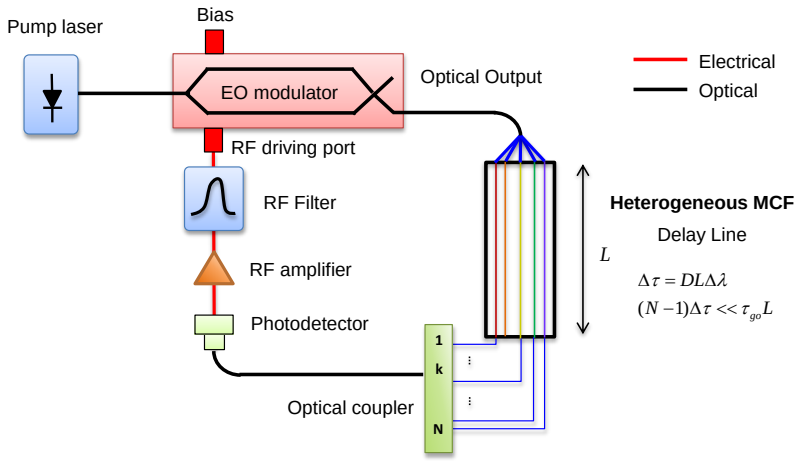

Fig. 30. Multi-cavity vernier OEO configuration using a heterogeneous MCF.

Reminding the concepts of the previous chapter, the time-delay of core *n* can be expressed by using Eq. (6) as:

$$\tau_n(\lambda) = \tau_{g0}L + nDL(\lambda - \lambda_0), \tag{27}$$

being D the common dispersion parameter and τ_{g0} the common group delay per unit length at a given anchor wavelength λ_0. In this case, Eq. (15) is transformed to:

$$\Phi_k = \omega\tau_{g0}L + k\omega DL(\lambda - \lambda_0) + \phi_k, \quad for\ k = 1,2,\dots,N. \tag{28}$$

Assuming $\phi_k = 0\ \ \forall k$, the oscillation frequency must verify:

$$f_0 = \frac{m}{\tau_{g0}L + DL(\lambda - \lambda_0)}. \tag{29}$$

For vernier operation at this frequency, we need:

$$f_0 DL(\lambda - \lambda_0) = 1. \tag{30}$$

Since the values of D are usually very small, the fulfillment of Eq. (30) will lead to multi-km cavity lengths, reaching lower phase-noise characteristics as compared to homogeneous MCF OEO designs. Designing the cores of the MCF as in the previous chapter, we can build up a TTDL which features, for example, τ_{g0} = 5 ns/m and D = 1 ps/km/nm. For an oscillating frequency of f_0 = 10 GHz, Eq. (30) determines that $L(\lambda - \lambda_0) = 10^5\ m \cdot nm$. Therefore, one possible solution is given by L = 5 km and $\Delta\lambda$ = 20 nm. Fig. 31 illustrates the oscillation spectra for this example when a heterogeneous 7-core fiber is considered and the number of parallel cavities ranges from 2 up to 7.

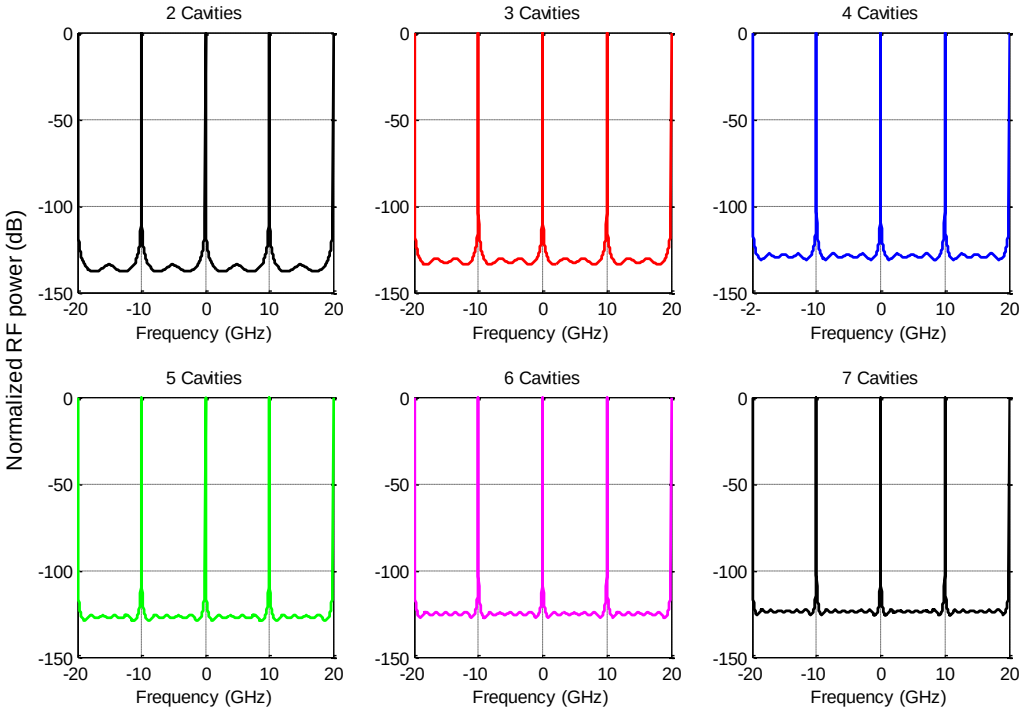

Fig. 31. Oscillation spectra for a multi-cavity vernier OEO using a 5-km 7-core heterogeneous MCF.

As it can be appreciated, in all cases the overall coupled cavity free spectral range is 10 GHz, despite the fact that the free spectral range values for the individual cavities are around 40 kHz. In consequence, mode selection does not require a selective RF filter since a bandwidth of 1 GHz is more than enough to select the 10-GHz oscillation resonance. It can be noted that increasing the number of cavities results in a reduction in the oscillation linewidth, as happened in the previous case. With respect to the phase noise spectra, Fig. 32 shows that the results are almost independent from the number of cavities, as these provide almost the same delay.

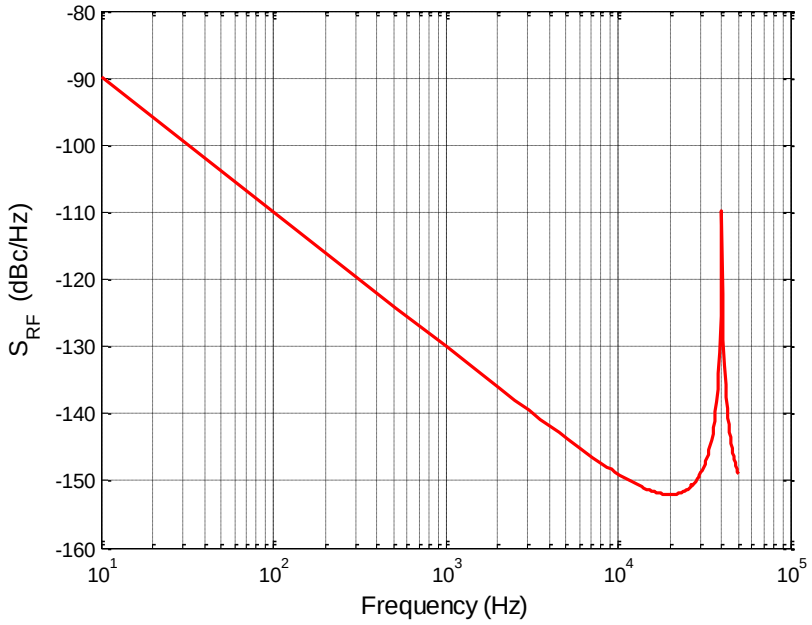

Fig. 32. Phase noise spectra computed for a multi-cavity vernier OEO based on a heterogeneous MCF.

A distinctive feature of this OEO, which follows from Eq. (30), is the possibility of tuning the oscillation frequency by changing $\Delta\lambda = \lambda - \lambda_0$, in other words, by using a tunable laser. For the example considered above, the specific relationship is f_o = 200 GHz / $\Delta\lambda$, where $\Delta\lambda$ is expressed in (nm). Fig. 33 shows this relationship (a) and the oscillation frequencies (b) in between 10 and 20 GHz, computed from Eq. (14) for a set of selected values of $\Delta\lambda$.

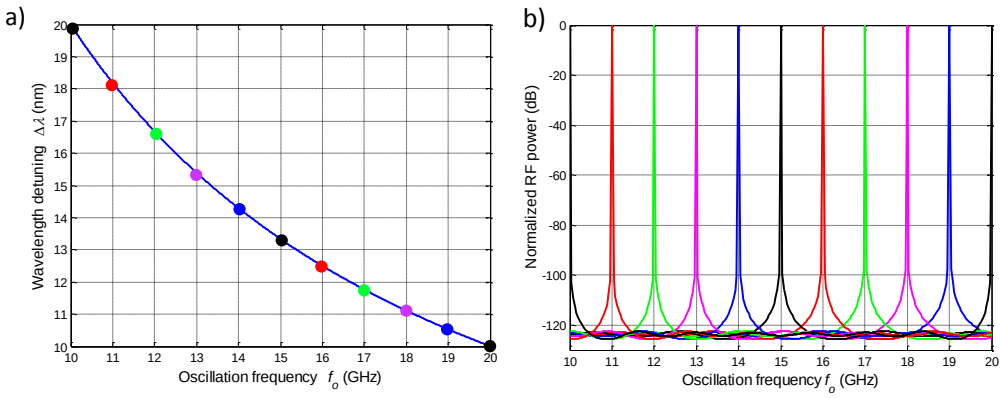

Fig. 33. Oscillation frequency versus wavelength detuning for a vernier multi-cavity OEO based on a 7-core heterogeneous MCF for τ_{g0} = 5 ns/m, D = 1 ps/km/nm and L = 5 km.

V. CONCLUSIONS

In this work, we have proposed a novel design procedure of true-time delay lines based on heterogeneous multicore fibers and one of their possible applications to an important MWP application such as optoelectronic oscillators. In addition to the well-known advantages associated to optical fibers, the inherent parallelism of MCFs makes them ideal candidates to build TTDLs in a single compact structure, providing an important reduction of size and weight as compared to similar structures based on single-core fibers. They also provide an ideal environment for the parallel propagation of signals subject to identical mechanical and environmental conditions, and thus can be considered for a wider range of application fields.

We have presented two different TTDL models based on 7-core heterogeneous MCFs, which differ by different refractive index profile of their cores: one is based on a step-index profile and the other is based on a trench-assisted step-index profile. The versatility of the second model allows us to modify 4 or even 5 design parameters instead of a pair of parameters as in the first one, which can be employed to extend the range of effective index values for the desired group index and dispersion range and thus reducing the inter-core crosstalk. A maximum inter-core crosstalk level of around -70 dB was reached in the first model while propagation over 1-km straight-link, which is in the order of the state-of-art values for heterogeneous MCFs. While propagating along the same straight-length with the second model, a crosstalk level below -100 dB was obtained, decreasing to a maximum value of -110 dB when the design procedure was optimized. When evaluating the

crosstalk behavior against curvatures, a threshold bending radius of 857 mm was obtained in the first model, while a quasi-bend insensitive design was reached in the second. Therefore, we conclude than the trench-assisted step-index profile can be an ideal candidate to implement low-crosstalk with low curvature-dependence TTDLs by using MCFs, even if the core-density has to be increased.

We then applied the proposed TTDLs to implement multi-cavity OEOs. Design equations and proposed examples have been presented, showing the potential of unique performance in terms of spectral selectivity, tunability and high-frequency operation. We first propose the use of homogeneous MCFs to build both unbalanced double-loop and multi-cavity vernier OEOs, and we observe that with a properly design of the cavities lengths high-spectral purity and multi-GHz oscillation mode spectral separation was obtained. On the other hand, OEOs based on heterogeneous MCFs allow for ultra-long cavity length (>1 km) compatibility with high-spectral purity lengths and multi-GHz oscillation mode spectral separation by using a vernier operation, while provide much lower phase noise operation. In addition, all of the proposed designs bring the potential of featuring the tunability of the oscillation frequency by feeding the OEO system with a wavelength-tunable laser.

ACKNOWLEDGEMENTS

The author wishes to acknowledge the financial support given by the Research Excellency Award Program GVA PROMETEO 2013/21 MICROWAVE PHOTONICS, TEC2014-60378-C2-1-R "FOTONICA DE MICROONDAS PARA APLICACIONES EMERGENTES".

REFERENCES

[1] A. J. Seeds and K. J. Williams, "Technology focus on Microwave photonics", Nat. Photonics, vol. 5, pp. 723-736, (2011).
[2] J. Yao, "Microwave Photonics", J. Lightwave Technol., vol. 27, no. 3, pp. 314-335, (2009).
[3] A. J. Seeds and K. J. Williams, "Microwave Photonics", J. Lightwave Technol., vol. 24, no. 12, pp. 4628-4641, (2006).
[4] J. Capmany, J. Mora, I. Gasulla, J. Sancho, J. Lloret, and S. Sales, "Microwave photonic signal processing", J. Lightwave Technol., vol. 31, no. 4, pp. 571-586, (2013).
[5] K. Wilner and A. P. van del Heuvel, "Fiber-optic delay lines for microwave signal processing", Proc. IEEE, vol. 64, no. 5, pp. 805-807, (1976).
[6] J. Capmany, D. Pastor, and B. Ortega, "New and flexible fiber-optic delay-line filters using chirped Bragg gratings and laser arrays", IEEE Trans. Microwave Theory Tech., vol. 47, no. 7, pp. 1321-1326, (1999).
[7] F. Zeng and J. Yao, "All-optical microwave filters using uniform fiber Bragg gratings with identical reflectivities", J. Lightw. Technol., vol. 23, no. 3, pp. 1410-1418, (2005).
[8] C.Wang and J. Yao, "Fiber Bragg gratings for microwave photonics subsystems", Opt. Express, vol. 21, no. 19, pp. 22868-22884, (2013).
[9] P. A. Morton and J. B. Khurgin, "Microwave photonic delay line with separate tuning of the optical carrier", Photon Technol. Lett., vol. 21, no. 22, pp. 1686-1688, (2009).

[10] D. Marpaung, C. Roeloffzen, R. Heideman, A. Leinse, S. Sales, and J. Capmany, "Integrated microwave photonics", Lasers Photon. Rev., vol. 7, no. 4, pp. 506-538, (2013).
[11] J. Sancho, J. Bourderionnet, J. Lloret, S. Combrié, I. Gasulla, S. Xavier, S. Sales, P. Colman, G. Lehoucq, D. Dolfi, J. Capmany, and A. De Rossi, "Integrable microwave filter based on a photonic crystal delay line", Nat. Communications, vol. 3, no. 1075, (2012).
[12] F. Ohman, K. Yvind, and J. Mork, "Slow light in a semiconductor waveguide for true-time delay applications in microwave photonics", Photon. Technol. Lett, vol. 19, no. 15, pp. 1145-1147, (2007).
[13] I. Gasulla and J. Capmany, "Microwave photonics applications of multicore fibers", IEEE Photonics J., vol. 4, no. 3, pp. 877-888, (2012).
[14] M. Koshiba, K. Saitoh, and Y. Kokubun, "Heterogeneous multi-core fibers: proposal and design principle", IEICE Electron. Express, vol. 6, no. 2, pp. 98-103, (2009).
[15] J. Tu, K. Saitoh, M. Koshiba, K.Takenaga, and S. Matsuo, "Optimized design method for bend-insensitive heterogeneous trench-assisted multi-core fiber with ultra-low crosstalk and high core density", J. Lightw. Technol. Vol. 31, no. 15, pp. 2590-2598, (2013).
[16] J. Tu, K. Saitoh, M. Koshiba, K. Takenaga, and S. Matsuo, "Design and analysis of large-effective-area heterogeneous trench-assisted multi-core fiber", Opt. Express, vol. 20, no. 14, pp. 15157-15170, (2012).
[17] T. Hayashi, T. Nagashima, O. Shimakawa, T. Sasaki, and E. Sasaoka, "crosstalk variation of multi-core fibre due to fibre bend", European conference on optical communication (ECOC) 2010, pp. 1-3, (2010).
[18] M. Koshiba, "Design aspects of multicore fibers for high-capacity long-haul transmissions", Int. Topical Meeting on Microwave Photonics (MWP) 2014, pp. 318-323, (2014).
[19] Y. Sasaki, Y. Amma, K. Takenaga, S. Matsuo, K. Saitoh, and M. Koshiba, "Investigation of crosstalk dependences on bending radius of heterogeneous multicore fiber", Optical Fiber Communication Conference (OFC/NFOEC) 2013, pp. 1-3, (2013).
[20] M. Koshiba, K. Saitoh, K. Takenaga, and S. Matsuo, "Multi-core fiber design and analysis: coupled-mode theory and coupled-power theory", Opt. Express, vol. 19, no. 26, pp. B102-B111, (2011).
[21] I. Kaminow, T. Li, A. Willner, "Optical fiber telecommunications volume VIA, components and subsystems", Academic Press, 6th Edition, chapters 9 and 13, (2013).
[22] W. Huang, "Coupled-mode theory for optical waveguides: an overview", J. Opt. Soc. Am. A, vol. 11, no. 3, pp. 963-983, (1994).
[23] T. Hayashi, T. Sasaki, E. Sasaoka, K. Saitoh, and M. Koshiba, "Physical interpretation of intercore crosstalk in multicore fiber: effects of macrobend, structure fluctuation, and microbend", Opt. Express, vol. 21, no. 5, pp. 5401-5412, (2013).
[24] J. Fini, B. Zhu, T. Taunay, and M. Yan, "Statistics of crosstalk in bent multicore fibers", Opt. Express, vol. 18, no. 14, pp. 15122-15129, (2010).
[25] M. Koshiba, "Design aspects of multicore optical fibers for high-capacity long-haul transmission", 2014 International Topical Meeting on Microwave Photonics (MWP) and 9th Asia-Pacific Microwave Photonics Conference (APMP), pp. 318-323, (2014).
[26] S. Garcia and I. Gasulla, "Design of Heterogeneous multicore fibers as sampled true-time delay lines", Opt. Letters, vol. 40, no. 4, pp. 621-624, (2015)
[27] S. Garcia and I. Gasulla, "Crosstalk-optimized multicore fiber true time delay lines", to be presented at 2015 International Topical Meeting on Microwave Photonics, Paphos, Cyprus (2015). Accepted.
[28] P. Watekar, S. Ju, and W. Han, "Design and development of a trenched optical fiber with ultra-low bending loss", Opt. Express, vol. 17, no. 12, pp. 10350-10363, (2009).
[29] X. S. Yao and L. Maleki, "Optoelectronic microwave oscillator", J. Opt. Soc. Am. B, vol. 13, no. 8, pp. 1725-1735 (1996).
[30] S. Garcia and I. Gasulla, "Multi-cavity optoelectronic oscillators using multicore fibers", Opt. Express, vol. 23, no. 3, pp. 2403-2415, (2015).
[31] X. S. Yao and L. Maleki, "Multiloop optoelectronic oscillator", IEEE J. Quantum Electron., vol. 36, no. 1, pp. 79-84, (2000).
[32] X. S. Yao and L. Maleki, "Converting light into spectrally pure microwave oscillation", Opt. Letters, vol. 21, no. 7, pp. 483-485, (1996).
[33] K. Volyanskiy, P. Salzenstein, H. Tavernier, M. Pogurmirskiy, Y. K. Chembo, and L. Larger, "Compact optoelectronic microwave oscillators using ultra-high Q whispering gallery mode disk-resonators and phase modulation", Opt. Express, vol. 18, no. 21, pp- 22358-22363, (2010).

ANNEX: PUBLICATIONS

1. S. Garcia and I. Gasulla, "Design of Heterogeneous multicore fibers as sampled true-time delay lines", Opt. Letters, vol. 40, no. 4, pp. 621-624, (2015).
2. S. Garcia and I. Gasulla, "Multi-cavity optoelectronic oscillators using multicore fibers", Opt. Express, vol. 23, no. 3, pp. 2403-2415, (2015).
3. S. Garcia and I. Gasulla, "Crosstalk-optimized multicore fiber true time delay lines", to be presented at 2015 International Topical Meeting on Microwave Photonics, Paphos, Cyprus (2015), (Accepted).
4. Sergi Garcia, Ivana Gasulla, "Application of Multicore fibers to Microwave Photonics", 36th Progress in Electromagnetics Research symposium, Prague, Czech Republic, (2015), (invited)

MWP justification of acceptance:

MWP 2015, 26-29 Oct 2015
2015 IEEE International Topical Meeting on Microwave Photonics

---

Author Notification 03 Aug 2015 16:00

Dear Sergi García,

The reviews for your submission to MWP2015 (*#65 Crosstalk-optimized multicore fiber true time delay lines*) have now been received and following their consideration at the recent TPC meeting we are pleased to inform you that your paper has been accepted for presentation as a **poster**. The overall quality of submissions was extremely high, hence we have not been able to accommodate all requests for oral presentations. We are putting the finishing touches to the technical program and hope to circulate this in the next few days along with further instructions pertaining to final preparation of papers for the proceedings.

We thank you for your contribution to what we anticipate to be an excellent technical program of wide-ranging interest and look forward to seeing you in Cyprus in October.

Best wishes,

Prof. Andreas Stöhr,
Chair of the TPC for MWP2015